Applied Thermal Engineering 302 (2026) 131967

Contents lists available at ScienceDirect

Applied Thermal Engineering

journal homepage: www.elsevier.com/locate/ate

Research Paper

Tri-hybrid transformer framework for multi-target performance prediction of solid desiccant evaporative cooling systems

Habeb Al-Sameai [a,b], Sibghat Ullah [c], Radhwan A.A. Saleh [d,e,*], Mustafa Ghaleb [d], Tauqir Nasir [f], Müslüm Arıcı [g], Zead Saleh [h], Muzaffar Ali [g,i]

[a] Institute of Natural and Applied Sciences, Erciyes University, Kayseri, Türkiye
[b] Department of Mechatronics Engineering, Taiz University, Taiz, Yemen
[c] Department of Mechanical Engineering, University of Management and Technology, Sialkot Campus, Lahore, Pakistan
[d] Department of Software Engineering, Engineering Faculty, Kocaeli University, 41001, Kocaeli, Türkiye
[e] Interdisciplinary Research Center for Construction and Building Materials, King Fahd University of Petroleum & Minerals (KFUPM), 31261, Dhahran, Saudi Arabia
[f] Department of Metallurgy and Materials Engineering, Engineering Faculty, Kocaeli University, 41001, Kocaeli, Türkiye
[g] Mechanical Engineering Department, Engineering Faculty, Kocaeli University, 41001, Kocaeli, Türkiye
[h] Department of Industrial Engineering, College of Engineering, University of Business and Technology, 21361, Jeddah, Saudi Arabia
[i] Energy Engineering Department, University of Engineering and Technology, Taxila, Pakistan

ARTICLE INFO

Keywords:
Solid desiccant evaporative cooling
Hybrid machine learning
Thermal system modeling
Adsorption dehumidification
Explainable AI
Thermal comfort

ABSTRACT

Solid desiccant evaporative cooling system (DECS) offers a sustainable alternative for building air conditioning; however, its coupled heat and mass transfer processes make accurate performance prediction challenging. Although data-driven models have increasingly been applied to this problem, existing approaches often suffer from limited prediction scope, reliance on single-paradigm architectures, insufficient evaluation of generalization capability, and limited interpretability. To address these challenges, this study proposes a Tri-Hybrid Transformer framework. The Tri-Hybrid Transformer integrates XGBoost leaf encodings, MLP-derived latent features, and raw inputs, which are concatenated and subsequently refined through a transformer-based attention module to capture higher-order feature interactions. The framework is validated using experimental data from an instrumented DECS operating under process air conditions of 30–40 °C and 12–20 g/kg, with regeneration temperatures ranging from 60 to 90 °C. Five-fold cross-validation yields R^2 values of 0.983 for $T_{s,out}$, 0.956 for $W_{s,out}$, 0.988 for CC, and 0.992 for COP. The proposed model consistently outperforms benchmark methods, including XGBoost, SVR, Random Forest, MLP, and Tabular Transformer. SHAP analysis further confirms physically consistent relationships between the input variables and the predicted outputs. These results demonstrate the potential of hybrid transformer-based models for accurate and interpretable prediction of DECS performance, enabling data-driven optimization of sustainable cooling technologies.

1. Introduction

The International Energy Agency (IEA) reports that the global economy is expected to grow at an annual rate of 3.4% over the next two decades [1]. Rapid economic expansion has significant social and economic implications, including increased urbanization, rising living standards, and greater use of energy-intensive appliances as populations transition from informal to formal housing [2]. As a result, it is estimated that, if the current pattern remains constant, energy demand in the building sector will increase by up to 60% by 2050 relative to 2007 [3]. At present, buildings are major consumers of electricity, accounting for approximately one-third of total global energy consumption [2]. In the building sector, most energy is consumed to meet human thermal requirements. To meet these needs, vapor-compression air-conditioning systems are extensively used. These systems require high energy to operate and also emit chlorofluorocarbons (CFCs), which contribute to global warming and other environmental effects. A low-cost, low-environmental-impact technological solution for air conditioning that also provides dehumidification is solid desiccant air-conditioning systems [4].

* Corresponding author at: Department of Software Engineering, Engineering Faculty, Kocaeli University, 41001, Kocaeli, Türkiye.
E-mail addresses: habeb.alsameai@taiz.edu.ye (H. Al-Sameai), sibghat.ullah@skt.umt.edu.pk (S. Ullah), radhwan.saleh@kocaeli.edu.tr (R.A.A. Saleh), mustafa.ghaleb@kocaeli.edu.tr (M. Ghaleb), tauqir.nasir@kocaeli.edu.tr (T. Nasir), muslumarici@kocaeli.edu.tr (M. Arıcı), z.saleh@ubt.edu.sa (Z. Saleh), muzaffar.ali@kocaeli.edu.tr, muzaffar.ali@uettaxila.edu.pk (M. Ali).

https://doi.org/10.1016/j.applthermaleng.2026.131967
Received 7 April 2026; Received in revised form 25 May 2026; Accepted 13 June 2026
Available online 19 June 2026
1359-4311/© 2026 The Authors. Published by Elsevier Ltd. This is an open access article under the CC BY license (http://creativecommons.org/licenses/by/4.0/).

Nomenclature

Abbreviations

AHU	Air handling unit
ANN	Artificial neural network
CC	Cooling capacity
COP	Coefficient of performance
DAC	Desiccant air conditioning
DEC	Direct evaporative cooler
DECS	Solid Desiccant evaporative cooling system
DW	Desiccant wheel
EES	Engineering Equation Solver
GA	Genetic algorithm
HRW	Heat recovery wheel
IEC	Indirect evaporative cooler
MAE	Mean absolute error
ML	Machine learning
MLP	Multilayer perceptron
NSGA-II	Non-dominated sorting genetic algorithm II
NZEB	Net-zero energy building
PV/T	Photovoltaic thermal
RBFNN	Radial basis function neural network
RF	Random forest
RMSE	Root mean square error
MSE	Mean square error
MAPE	Mean absolute percentage error
MedAE	Median absolute error
EV	Explained variance score
MBD	Mean bias deviation
R^2	Coefficient of determination
Adj R^2	Adjusted coefficient of determination
SHAP	SHapley Additive exPlanations
SVR	Support vector regression
TRNSYS	Transient system simulation tool
XGBoost	Extreme gradient boosting

Variables

T	Temperature (°C)
W	Humidity ratio (g/kg)
h	Enthalpy (kJ/kg)

Performance indicators

CC	Cooling capacity (kW)
COP	Coefficient of performance (-)

Subscripts

in	Inlet
out	Outlet
dw	Desiccant wheel
hw	Heat recovery wheel
reg	Regeneration
s	Supply air

Greek symbols

μ	Mean value
σ	Standard deviation
ϵ	Small constant to avoid division by zero

Machine learning variables

$x^{(s)}$	Standardized variable
x_i	Input feature vector
y	Target variable
y_i	True target value
$\hat{y}_i$	Predicted value
$\bar{y}$	Mean of target values
n	Number of samples
p	Number of predictors

Model variables

ℓ_i	Leaf index vector (XGBoost output)
$z_i^{(\text{leaf})}$	One-hot encoded leaf vector
$z_i^{(\text{nn})}$	Neural network latent representation
r_i	Projected raw input representation
u_i	Projected tree-based representation
v_i	Projected neural representation
$h_{0,i}$	Fused feature representation
$h_{1,i}, h_{2,i}$	Attention-refined representations

Operators

MHA	Multi-head attention mechanism
LN	Layer normalization
Var(·)	Variance operator

Desiccant air conditioning systems can handle sensible and latent loads separately. To control the latent load, a rotor called a desiccant wheel (DW) is used [5]. The DW is designed with special features that efficiently dehumidify the ambient air entering the desiccant air conditioning system. The DW not only removes humidity from the air but also can absorb a large amount of moisture [6]. It is essential to highlight the difference between holding and adsorption of moisture. When humid air passes through materials, most of them are capable of holding moisture in the form of surface wetting or temporary retention. However, materials with specific porous and hygroscopic properties are capable of adsorbing moisture from the air. Desiccant materials require thermal energy to be regenerated for continuous operation [7]. Solar thermal collectors are an attractive option to provide the required energy that can reactivate the DW. The use of solar thermal systems or waste heat makes desiccant systems environmentally friendly and cost-effective. In addition, integration of an evaporative cooler, either direct or indirect, with the DW is necessary to cover the sensible load [8].

Several numerical and experimental studies have evaluated the performance of solar-assisted desiccant evaporative air-conditioning systems at both the component and system levels with various configurations [9]. A comparative study conducted under Mediterranean climate conditions proved that DW air dehumidification can provide primary energy savings of 20 to 25% and achieve up to a 40% reduction in carbon dioxide emissions compared with traditional air-conditioning systems [10]. Similarly, Elmer et al. [11] used potassium formate as a desiccant material to evaluate the thermal and electrical coefficient of performance (COP) of a desiccant air-conditioning unit installed in a building with a cooling load of 1362 W. Results revealed that the thermal and electrical COP achieved from the system were 1.26 and 3.67, respectively. A TRNSYS simulation model was developed for four different configurations of solar desiccant cooling systems under the climate conditions of two major cities in Pakistan, Lahore and Karachi. Results revealed that a high COP was achieved when an indirect evaporative cooler (IDEC) was used for precooling and a direct evaporative cooler (DEC) was used for post-cooling [12]. The effect of process air conditions, such as humidity and temperature, was

experimentally analyzed to evaluate the performance of pre-cooling the DW. The effectiveness and energy-saving potential of this design can be useful for developing desiccant-based air-conditioning systems under various climates around the world [13]. Similarly, a numerical simulation study was conducted to evaluate the performance of a solar-driven desiccant-based IDEC for buildings. It was found that when IDEC is integrated with a desiccant system, it can significantly decrease the sensible cooling load and increase the level of thermal comfort [14]. Lin et al. [15] experimentally validated a computational model to investigate the performance of an evaporative cooling system coupled with a dehumidifier. Muthu et al. [16] analyzed the behavior of the DW by varying the area of the regeneration side. It was highlighted that under identical operating conditions, when the area of the process side was decreased and the area of the regeneration section was increased, a higher moisture removal rate and a rise in the temperature of the process outlet air were achieved. Tian et al. [17] employed an integrated experimental and simulation approach to study the performance of a heat-pump-assisted single-stage desiccant-wheel system throughout the year in a near-zero-energy residential building. A new parameter, the wet energy ratio, was proposed in the study to determine the optimal outlet air temperature of the evaporator for pre-cooling during both hot and humid seasons. The results showed that the proposed arrangement improves thermal comfort in the building compared with traditional air-conditioning systems and lowers energy demand. Ma et al. [18], in a similar study, assessed the performance of deep dehumidification systems used in a lithium-ion battery manufacturing plant. The COP of the dehumidification process ranged between 0.54 and 0.63 during normal winter operation, while a much higher range of 1.15 to 1.25 was obtained during summer operation. Bulck et al. [19] experimentally studied the effect of process and regeneration air mass flow rate, inlet temperature, and inlet humidity ratio on the operation of a solid desiccant cooling system. The findings revealed that operating the system at high regeneration temperatures can greatly reduce the air flow rate required on both the process and regeneration sides. These studies collectively highlight the progress in modeling and performance evaluation of solid desiccant cooling systems under diverse operating conditions.

Despite these advances, several limitations remain in the existing literature. Conventional analytical and experimental methodologies exhibit inherent limitations. Physics-based models require extensive geometric and operating parameters that may be unavailable in practice, while their predictive accuracy often remains constrained. Experimental campaigns, while valuable, are resource-intensive and time-prohibitive for comprehensive parametric exploration. These limitations have motivated the exploration of artificial intelligence (AI) techniques, which offer computationally efficient alternatives for modeling complex system behavior without requiring explicit analytical formulations [20]. Once trained on sufficient data, AI techniques can accurately predict system outputs while substantially reducing computational burden and experimental requirements.

Review studies have highlighted the growing importance of intelligent and hybrid modeling approaches for predicting the performance of solid desiccant cooling systems and improving thermal comfort in building applications [21,22]. For instance, Artificial Neural Networks (ANNs) have proven highly effective in modeling complex thermal systems by learning the underlying nonlinear relationships within high-dimensional data [20]. Zendehboudi et al. [23] successfully predicted DW performance using experimental inputs including regeneration temperature, flow rate ratios, wheel diameter, and rotational velocity, identifying optimal operating points for various wheel sizes. Comino et al. [24] achieved mean square errors of 0.39 in predicting outlet temperature and humidity for low-temperature regeneration wheels (below 52 °C) using an ANN model. Similar ANN-based methodologies have been successfully applied to hybrid desiccant-vapor compression systems [25], silica-gel wheels [26], and other related systems [27], consistently outperforming simplified physical models. Antonellis et al. [28] developed data-driven correlations from experimental data that forecast variations in process-air temperature and humidity ratio within a 10% error margin.

Table 1 presents a comprehensive synthesis of recent desiccant air-conditioning studies, systematically categorized by system configuration, methodological approach, and key findings. This compilation reveals important patterns in the evolution of the field and highlights persistent gaps in current research. The table reveals four critical limitations that constrain the current state of AI-enhanced DECS modeling.

First, existing studies predominantly predict a narrow set of outputs — typically outlet temperature, humidity ratio, or COP — rather than the comprehensive thermodynamic indicators required for system-level evaluation. Simultaneous prediction of supply temperature ($T_{s,out}$), supply humidity ratio ($W_{s,out}$), cooling capacity (CC), and COP remains unexplored. These metrics exhibit fundamentally different nonlinear dependencies and are governed by distinct state descriptors, with temperature-humidity states contrasting with enthalpy-based quantities, thereby posing substantial challenges for models developed within constrained operating envelopes.

Second, the predominant reliance on single-paradigm predictors — whether multi-layer perceptrons (MLP/ANN) or tree-based regressors — fails to adequately capture the mixed behavioral characteristics of adsorption-driven cooling systems. While MLPs excel at learning smooth nonlinear mappings, they struggle with the regime-dependent dynamics inherent in adsorption–desorption processes. Conversely, tree-based models effectively capture structured partitioning in tabular data but lack continuous latent representation learning capabilities. Transformer architectures, despite their powerful attention mechanisms for modeling feature interactions, typically underperform when applied directly to small-to-medium experimental tabular datasets, necessitating hybrid designs in which attention serves feature fusion rather than standalone prediction.

Third, the overwhelming majority of investigations fail to implement rigorous validation protocols that demonstrate model robustness on unseen data and guarantee generalization capability. Among the studies reviewed in Table 1, only [24] employed k-fold cross-validation to verify that predictive performance holds beyond the training dataset. This omission is particularly problematic for desiccant cooling systems, which exhibit strong seasonal variations and operate across wide-ranging ambient conditions.

Fourth, a related interpretability deficit pervades AI-enhanced thermal studies. Performance reporting rarely extends beyond aggregate error metrics to quantify how key operating variables, particularly regeneration temperature (T_{reg}), inlet humidity ratio, and enthalpy-related states, contribute to predicted outputs. This opacity compounds the generalization problem, as stakeholders cannot determine whether predictions remain physically plausible when extrapolating beyond training distributions. The combination of limited generalization validation and absent interpretability constrains engineering trust and diminishes practical utility for diagnosis, optimization, and control-oriented decision-making, ultimately limiting the translational value of data-driven approaches for real-world system implementation.

Unlike prior studies that address only one or two of the above limitations, the present work introduces a comprehensive framework that simultaneously tackles all four gaps. The specific novelties are detailed below with direct comparisons to existing literature. First, to overcome the narrow output prediction common in existing literature, the present work develops separate, optimized models for four distinct thermodynamic metrics that have never been simultaneously applied to solid desiccant systems. Second, while prior studies rely exclusively on single-paradigm models (MLP/ANN or tree-based regressors), the present work proposes a novel tri-hybrid attention-based fusion architecture combining XGBoost leaf encodings, MLP-derived hidden features, and raw inputs refined via transformer attention, representing the first application of such hybrid feature fusion to desiccant cooling.

Table 1
Comprehensive synthesis of desiccant air conditioning research: System configurations, methodological approaches, and research gaps in AI integration, generalization, and explainability.

Ref./ Year	Nature of work	System configuration	Methodology	Key findings	XAI	Gen.
[29]/ 2018	Simulation + Optimization	Solid DAC + indirect evaporative cooling	Optimization and parametric analysis.	COP improved 20% via optimized speed and T_{reg}. High wheel speed reduced dehumidification effectiveness.	No	No
[24]/ 2019	Experimental + Machine Learning	Solid DW using low T_{reg}.	Multi-task ANN validation using experimental datasets.	Multi-task ANN modeled performance with < 5% error. Low-grade heat (< 60° C) confirmed as feasible.	No	Yes
[30]/ 2021	Simulation	Hybrid DAC + direct/indirect evaporative coolers	MATLAB-Simulink optimization and validation.	30%–45% latent load reduction and 20%–35% energy savings. Average COP of 0.6–0.8 achieved.	No	No
[17]/ 2021	Simulation + Optimization	Solid DAC system + heat-pump in NZEBs.	Parametric optimization and dynamic modeling.	Enhanced humidity control in NZEBs. Optimized T_{reg} and airflow ratios reduced annual energy consumption.	No	No
[31]/ 2026	Simulation	Solid DAC using low T_{reg}.	System-level thermodynamic modeling.	COP 0.9–1.2 achieved using low-grade heat sources (< 60° C). Validated solar/waste heat integration.	No	No
[32]/2022	Simulation	Solid DAC + direct/indirect evaporative coolers	EES thermodynamic modeling.	COP (0.22–0.78) highly sensitive to ambient humidity and indoor set temperature.	No	No
[6]/ 2023	Experimental	Solid DAC + direct evaporative cooler.	Experimental performance analysis.	Max COP 1.06 at 60 °C T_{reg}. Supply conditions heavily influenced by inlet temperature and humidity.	No	No
[33]/ 2023	Simulation	Solid DAC + direct/indirect evaporative coolers	Hourly seasonal modeling.	COP range 0.46–4.09. Solar PV/T integration significantly boosted moisture handling capacity.	No	No
[34]/ 2023	Experimental	Solid DAC with energy recovery.	Lab prototype testing.	Thermal COP 3.68, electrical COP 3.79. Energy savings of 21.9%–28% achieved via heat recovery.	No	No
[35]/2023	Machine Learning	Transient DECS.	ANN + GA optimization.	ANN predicted performance ($R^2 > 0.98$). NSGA-II optimization reduced water footprint to 45.17 kg/h.	Yes	No
[18]/ 2024	Experimental + Optimization	Solid DAC in battery manufacturing plant.	Operational optimization and on-site measurements.	Achieved ultra-low humidity (< 1.5 g/kg). 18%–26% energy efficiency gain after optimization.	No	No
[20]/ 2024	Simulation + Machine Learning	Solar-assisted solid DAC system.	RBFNN modeling.	RBFNN predicted performance ($R^2 > 0.97$). ML enabled real-time prediction and reduced computational costs.	No	No
[36]/ 2024	Simulation + Machine Learning	Solid DAC integrated with Maisotsenko Cycle.	Thermodynamic modeling + ANN + Bayesian optimization.	18%–25% COP increase. ML captured nonlinear heat/mass coupling with $R^2 = 0.99$.	Yes	No
[37]/ 2024	Experimental + Simulation	Solid DAC system (Algeria).	TRNSYS simulation and validation.	Simulated COP (1.13) validated against experimental (1.08). 65% rotary heat exchanger efficiency.	No	No
[38]/ 2024	Experimental	Water-assisted regeneration DW.	Controlled lab experimentation.	Condensing regeneration enhanced desorption and reduced thermal input under high latent loads.	No	No

(*continued on next page*)

Table 1 (*continued*).

[39]/ 2024	Simulation	Solar-assisted DAC + indirect evaporative cooler.	System modeling (humid climates).	Cooling effectiveness > 1. Solar-integrated IEC improved performance in high-humidity regions.	No	No
[40]/ 2024	Experimental	Integrated desiccant dehumidifier & dew-point cooler.	Pilot-scale tests and parametric analysis.	Achieved high electric COP of 6.43. Integrated design is efficient and environmentally friendly.	No	No
[41]/ 2025	Machine Learning	Solid DAC integrated with Maisotsenko Cycle.	RBFNN modeling.	High prediction accuracy ($R^2 > 0.97$) achieved using RBFNN and real-time experimental data.	No	No
[42]/ 2026	Simulation	Hybrid models using two solid DWs.	Thermodynamic optimization.	Thermal COP of 1.32 achieved at 85 °C T_{reg} for a 57.2 kW cooling load.	No	No

Note: XAI (Explainable AI) refers to the use of techniques (such as SHAP, LIME, white-box mathematical extraction, or physical sensitivity analysis) to make the internal workings and feature importance of the AI models interpretable. Gen. (Generalization) refers to the rigorous validation of the AI model's ability to perform robustly on unseen data, specifically through techniques like k-fold cross-validation or multiple independent runs.

Third, while existing literature exhibits a clear gap in robust validation, this study implements a rigorous 5-fold cross-validation protocol across all stages of model development. By reporting fold-averaged metrics alongside their corresponding standard deviations, we provide a statistical guarantee of model generalization that is absent from prior works. Fourth, while prior AI studies on desiccant systems rely heavily on black-box AI methodologies without physical validation, the present study uniquely leverages SHAP (SHapley Additive exPlanations) analysis to resolve this limitation. Fifth and finally, while individual elements exist separately in prior work, the integrated combination of multi-target prediction, tri-hybrid attention-based fusion, rigorous cross-validation, and SHAP interpretability within a single framework establishes an unprecedented benchmark for trustworthy AI in desiccant air-conditioning systems, demonstrating that data-driven methods can simultaneously achieve high accuracy and practical transparency. The main contributions are summarized as follows:

- **Multi-target thermodynamic prediction:** Rather than pursuing a monolithic predictor, we develop separate models for four critical metrics, $T_{s,out}$, $W_{s,out}$, cooling capacity (CC), and COP, each trained on experimental data with target-optimized input features. This approach acknowledges the distinct physics governing each output, enabling specialized representation learning unattainable through shared architectures.
- **Tri-hybrid attention-based feature fusion:** We propose a fusion architecture combining three complementary representations: (i) XGBoost leaf encodings capturing regime-aware structural partitioning of adsorption–desorption transitions; (ii) MLP-derived hidden features learning continuous nonlinear transformations; and (iii) raw input features preserving original information. These representations are concatenated into a unified embedding, which is subsequently refined by a transformer-based attention module to model higher-order feature interactions across diverse operating conditions.
- **Rigorous generalization validation:** To address the generalization gap documented in the literature, we implement 5-fold cross-validation throughout model development. All performance metrics are reported as fold-averaged values with standard deviations, providing statistical confidence intervals that demonstrate robustness across experimental data subsets.
- **Physically-interpretable predictions via SHAP:** We integrate SHAP analysis to quantify marginal contributions of key operating variables — regeneration temperature (T_{reg}), inlet humidity ratio, process air velocity, and ambient temperature — to individual predictions. This transparency enables physical validation, model diagnosis, and informed optimization decisions.
- **New benchmark for trustworthy AI in thermal engineering:** The integration of multi-target prediction, hybrid feature fusion, rigorous validation, and interpretability establishes a methodological benchmark demonstrating that data-driven approaches can achieve both high accuracy and the transparency required for practical deployment.

The remainder of this manuscript is organized as follows: Section 2 describes the experimental DECS configuration and data acquisition methodology. Section 3 presents the theoretical foundations and architectural details of the proposed Tri-Hybrid Transformer framework and elaborates on implementation methodology, including data preprocessing, training protocols, cross-validation strategies, and evaluation metrics. Section 4 reports and discusses the experimental results, including comparative performance analysis, and SHAP-based interpretability. Section 5 synthesizes key conclusions and outlines future research directions.

2. The system description

In the current work, the desiccant evaporative system consists mainly of a DW coated with silica gel, a heat recovery wheel (HRW), a DEC, an electric heater, and water pumps, as shown in the schematic diagram (Fig. 1). The silica gel coating was selected due to its high moisture adsorption capacity, favorable cyclic stability, and relatively low regeneration temperature requirements. The desiccant wheel used in the experimental setup had a moisture removal capacity of 19 kg/h, while silica gel was employed as the adsorbent material due to its favorable adsorption characteristics for desiccant cooling applications. Silica gel typically exhibits a bulk density in the range of 650–750 kg/m^3, thermal conductivity of approximately 0.15–0.20 W/m·K, and adsorption capacity ranging between 0.25–0.40 kg water/kg desiccant depending on operating conditions. These characteristics make silica gel suitable for solid desiccant cooling applications operating under moderate regeneration temperatures. The DW is used to dehumidify the moist outdoor air entering the system at points 1–2. After passing through the DW, the air becomes dehumidified and gains some temperature due to the heat released during the adsorption process. This hot and dry air then passes through the HRW at points 2–3. The heat recovery wheel acts as a pre-cooler. At this stage, heat is transferred from the dehumidified air to the regeneration air stream, cooling the air before it enters the DEC. After that, the pre-cooled and dry air passes through the DEC at points 3–4. At this stage, the dehumidified air flows over the wetted surface of the cooling pad. Due to the evaporation process, heat is absorbed from the process air, lowering its temperature. At this stage, the system is able to provide the required air to achieve human thermal comfort. The test room is connected to the DECS using

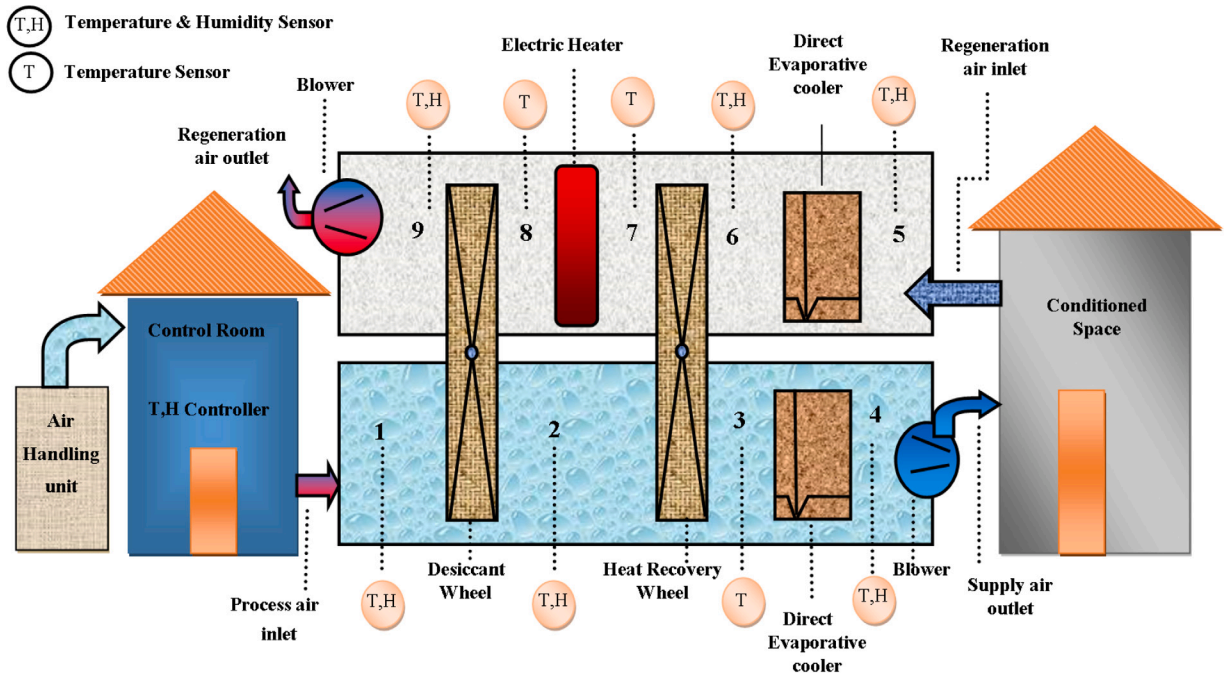


Fig. 1. Schematic representation of the DECS configuration, illustrating the major system components and airflow paths.

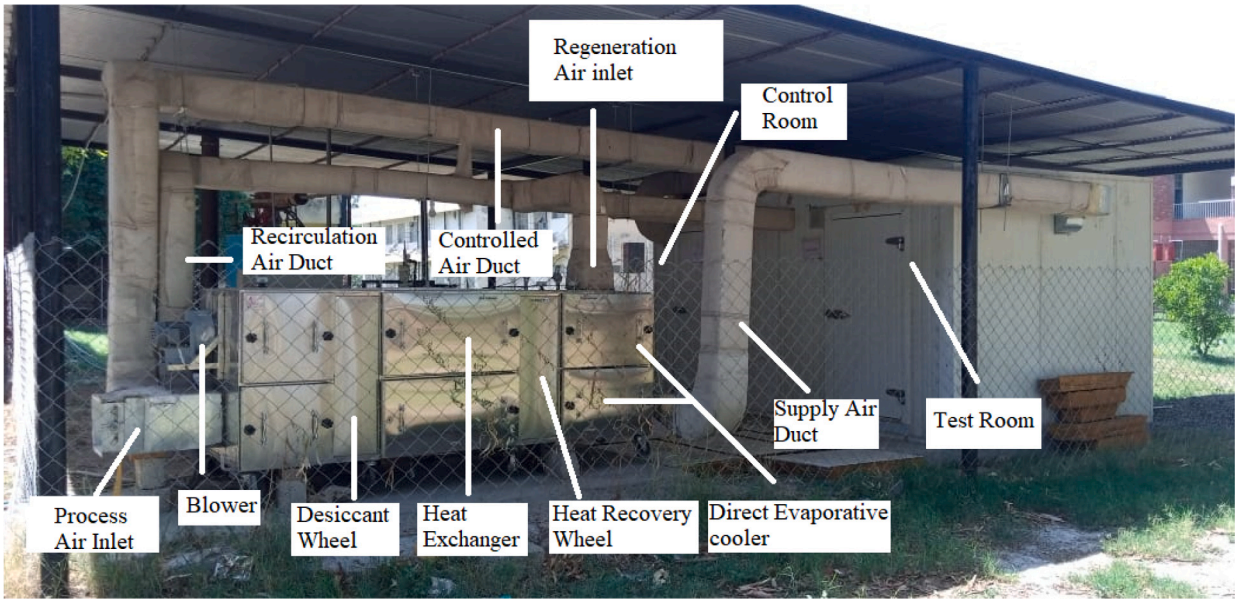


Fig. 2. Experimental setup and data acquisition system of the proposed DECS.

a duct to evaluate the system performance under a wide range of operating conditions.

On the other side, which is the regeneration side of the system, another DEC is installed to provide cool ventilated air to the HRW at points 5–6. The HRW acts as a rotary heat exchanger at points 6–7, whereas at points 7–8, electric heaters are installed to provide hot air to the DW for regeneration. Finally, at points 9–10, the DW is reheated and desorbed for continuous operation. Suction fans are installed on both sides to provide the required air flow rate. The specifications of each component are summarized in Table 2.

Despite their advantages in humidity control and energy-efficient cooling, solid desiccant evaporative cooling systems (DECS) exhibit several practical limitations. These systems generally require relatively large installation space due to the integration of multiple components such as the desiccant wheel, heat recovery wheel, and evaporative cooling units. In addition, their performance strongly depends on the availability of suitable regeneration heat sources and is highly sensitive to operating conditions, including inlet air temperature, humidity ratio, regeneration temperature, and airflow rate. The control and operation of DECS may also become complex under varying climatic conditions, requiring careful monitoring and adjustment to maintain stable performance.

2.1. Experimental setup

In this work, a robust experimental setup was developed with proper instrumentation and a data acquisition system for extensive experimentation under a wide range of inlet ambient conditions as shown in Fig.

Table 2
Specifications of components of the system.

Component	Parameter	Specification
Desiccant Wheel (DW) with Cassette	Model No.	KM-0058
	Type	Rotary type
	Dehumidification Capacity	19 kg/h
	Absorbent Material	Silica Gel
	Size	700 × 200 mm
	Capacity	1000–2000 CFM (≈ 1700–3400 m^3/h)
	Moisture Removing Capacity	Inlet up to 22 g/kg
		Outlet 10–12 g/kg
Heat Recovery Wheel (HRW) with cassette	Type	Rotary type
	Size	700 × 200 mm
	Capacity	1000–2000 CFM (≈ 1700–3400 m^3/h)
	Fin Thickness	0.12 mm
	Materials	Aluminum and 3A Molecular sieve
Fan	Type	Centrifugal
	Material of Blades	Aluminum
	Inlet Diameter	183 mm
	Air Capacity	1500–3500 m^3/h
Auxiliary Electric Heater	Power	0.5–15 kW
	Temperature Range	60–120 °C
	Material	Stainless steel
Air Handling Unit (AHU)	Range of Temperature	10–50 °C
	Tonnage capacity	8.8 kW
	RH	95%

2. The design capacity of the system is 7 – 10 kW (2 – 3 tons) with the variable air flow rate of 1700 – 3400 m^3/h (1000 – 2000 CFM). All components are selected accordingly, including DW, HRW, DEC, electric heaters, and fans, as the specifications are given in Table 2. The performance of the system was analyzed by varying key operating parameters, including humidity ratio, inlet air temperature, regeneration temperature, and air flow volume rate. Input conditions at the supply side were supplied from the control room to test the system under different climate scenarios. Specifically, the system was tested with the process-side air inlet temperature ranging from 30 to 40 °C and the inlet humidity ratio varying between 12 and 20 g/kg. The air flow volume rate was maintained at 1700 m^3/h for both the process and regeneration sides. The control room was used to provide the desired inlet conditions at the inlet of the DW. An air handling unit (AHU) was connected to the control room to maintain the temperature and humidity artificially. A test room was also connected to the outlet of the system to validate the system's performance under varying operating conditions. Thermal comfort inside the conditioned space was maintained by continuously supplying cooled and dehumidified air generated by the DECS through insulated supply ducts connected to the test room. The inlet air conditions were controlled using a dedicated control room to simulate different operating scenarios. In the proposed system, latent and sensible cooling loads were handled separately using the desiccant wheel and direct evaporative cooler, respectively. Key operating parameters influencing indoor thermal comfort included regeneration temperature, airflow rate, supply air temperature, and supply air humidity ratio, which collectively governed the stability and effectiveness of the indoor cooling conditions. Based on the inlet ambient conditions, regeneration temperatures between 60 and 90 °C were employed throughout the analysis. To ensure experimental consistency, upon completion of each experimental scenario, the system was reset to its initial operating inlet conditions before proceeding to the next experimental case.

2.2. Instrumentation and measurement procedure

To evaluate system performance at different stages, temperature and humidity sensors are installed at various points. Pt-100 sensors are used to record air temperature, and PHT 3109 sensors are used to record air humidity at different points on the test rig. All sensor readings are recorded through the Human–Machine Interface (HMI) screen. A programmable logic controller (PLC) is used to operate each component of the system. The PLC controls the on/off operation of fan blowers, DW, HRW, water pumps, and electric heaters. The rotational speeds of the DW and the blower fan are varied and controlled by the PLC. Table 3 presents the specifications of the sensors. Initially, all installed sensors are calibrated against standard temperature and humidity sensors available in the university laboratory. An offset is adjusted in the installed sensors of the test rig with reference to the standard sensors.

Experimental measurements are subject to uncertainties arising from instrument precision, environmental fluctuations, calibration limitations, and operational variations during data acquisition. To minimize these effects, all sensors were calibrated prior to experimentation, and repeated measurements were conducted under controlled operating conditions. To assess the reliability of the measured and derived performance parameters, an uncertainty analysis was conducted using the Root Sum Square (RSS) method based on the error propagation approach proposed by Kline and McClintock [43] and commonly presented in experimental engineering analysis literature [44].

Let, $y = f(x_1, x_2, x_3, \ldots)$

$$W_y = \sqrt{\left(\frac{\partial y}{\partial x_1} W_{x_1}\right)^2 + \left(\frac{\partial y}{\partial x_2} W_{x_2}\right)^2 + \left(\frac{\partial y}{\partial x_3} W_{x_3}\right)^2 + \cdots + \left(\frac{\partial y}{\partial x_n} W_{x_n}\right)^2} \quad (1)$$

where W_y represents the total uncertainty associated with the calculated parameter y, x_i denotes the independent measured variables, and W_{x_i} corresponds to the uncertainty associated with each measuring instrument. The uncertainties associated with all measuring devices used in this study are summarized in Table 3.

Based on the uncertainty propagation analysis, the overall uncertainty associated with the thermal COP of the DECS system was estimated to be approximately 9.16%.

The thermodynamic variables measured at the instrumented locations constitute the input–output feature set used for the data-driven modeling framework described in Section 3. The structured experimental design ensures that the machine learning models are trained and validated on physically consistent operating conditions representative of real DECS behavior.

Table 3
Specifications of measuring instruments.

Measurement	Measuring instrument	Measuring range	Accuracy
Temperature	Pt-100	−10–100 °C	±0.15°C
Relative humidity	PHT 3109	0%–99%	±2%
Air flow rate	Anemometer	0.1–20 m/s	±0.01 m/s
Water temperature	K-type Thermocouple	0–200 °C	0.3%
Water flow rate	Flow transducers	0.1–120 LPM	±5%

3. Methodology

The overall methodology adopted in this study is illustrated as a flowchart in Fig. 3. The workflow begins with the design and experimental implementation of the DECS, followed by systematic data acquisition under varying operating conditions. The collected dataset is then used to train and benchmark multiple regression models within a standardized nested cross-validation and hyperparameter tuning framework. A novel Tri-Hybrid Transformer is proposed to fuse tree-based, neural, and attention representations for improved nonlinear learning. Finally, predictive performance and interpretability are evaluated using comprehensive statistical metrics and SHAP-based feature importance analysis. The experimental dataset used in this study was collected under controlled operating conditions. The ranges of the key operating parameters are summarized in Table 4.

3.1. Experimental design and case studies

In this study, four experimental case studies (Exp 1–Exp 4) were conducted to evaluate the predictive performance of the model across multiple thermodynamic outputs and system-level performance indicators. Exp 1 focuses on predicting the supply air temperature ($T_{s,out}$) based on desiccant-wheel inlet/outlet states and regeneration conditions. Exp 2 targets the supply humidity ratio ($W_{s,out}$), utilizing the desiccant-wheel inlet/outlet variables and the regeneration temperature. Exp 3 estimates the cooling capacity (CC) using the process inlet states together with enthalpy-based variables. Exp 4 predicts the coefficient of performance (COP), employing the most comprehensive set of thermodynamic states spanning both the supply and regeneration streams. A summary of all cases, including the specific input feature sets and their corresponding targets, is provided in Table 4.

Separate models were trained for each target variable to avoid representation interference and to allow target-specific feature learning aligned with the distinct thermodynamic relationships governing each output.

3.2. Machine learning benchmarks and data preprocessing

To model the nonlinear thermodynamic behavior of the experimental DECS, six regression architectures were evaluated: Random Forest (RF) [45], Extreme Gradient Boosting (XGBoost) [46], Support Vector Regression (SVR) [47], an artificial neural network (ANN/MLP) [48], a Tabular Transformer [49], and the proposed Tri-Hybrid Transformer. These benchmarks were selected to represent complementary modeling philosophies on tabular data. Tree-based ensembles (RF and XGBoost) capture nonlinear feature interactions through hierarchical partitioning; SVR provides a margin-based regression baseline with strong regularization; the MLP serves as a standard neural approximator for smooth nonlinear mappings; and the Tabular Transformer evaluates whether self-attention can effectively learn higher-order dependencies from structured thermodynamic measurements.

Prior to training, each experimental dataset was organized into input features and a target variable, and column names were cleaned to remove formatting inconsistencies. Because the measured inputs span different physical units and numerical ranges (e.g., temperature in °C and humidity ratio in g/kg), all input variables were standardized via z-score normalization using statistics computed from the training split of each fold:

$$x^{(s)} = \frac{x - \mu}{\sigma}, \tag{2}$$

where μ and σ denote the mean and standard deviation of a given feature. The same transformation was then applied to the corresponding validation/test partitions to prevent data leakage. The target variable was also standardized during training to enhance numerical stability and convergence, with predictions subsequently inverse-transformed to their original units for reporting evaluation metrics. Model performance was assessed using k-fold cross-validation to ensure robust generalization and fair comparison under identical preprocessing and evaluation conditions. All experiments were conducted using a fixed random seed (seed = 42) to ensure reproducibility across cross-validation folds. A total of 14,724 experimental samples were collected across four independent experimental cases, each comprising 3681 samples. To ensure rigorous model evaluation and avoid overfitting, a 5-fold cross-validation strategy was employed throughout all stages of model development. In this strategy, the entire dataset for each independent experimental case was randomly partitioned into five mutually exclusive subsets (folds) of approximately equal size. This 5-fold cross-validation protocol ensures that data leakage between training and testing sets is completely prevented, as samples from the same fold never appear simultaneously in both training and testing within a given run. Furthermore, the model's generalization capability is assessed on unseen data within each case, and the final performance metrics are reported as fold-averaged values with standard deviations, providing statistical confidence in the results.

Since no single learning algorithm is consistently optimal across all operating regimes, the benchmark set spans partition-based, margin-based, and representation-learning approaches. This comparison helps identify which inductive biases best align with the coupled heat and mass transfer mechanisms of the DECS cycle. Building on these observations, the following section introduces the proposed Tri-Hybrid Transformer, which combines regime-aware structure (tree leaves), continuous latent representations (MLP features), and attention-based fusion within a unified framework.

3.3. Tri-hybrid transformer: Proposed tree–neural–attention fusion model

The proposed *Tri-Hybrid Transformer* is a hybrid regression framework developed for experimental tabular data in which system behavior is highly nonlinear and varies across operating regimes. The model integrates three complementary representation sources within a single predictor: (i) structured decision-path information extracted from an XGBoost regressor, (ii) continuous latent features learned by a feedforward neural network (MLP), and (iii) a Transformer-based attention refinement module applied to the fused representation to model higher-order feature interactions, as shown in Fig. 4. This design is motivated by the fact that boosted trees are highly effective for structured tabular patterns, MLPs provide continuous nonlinear representation learning, and attention-based fusion can emphasize the most informative representations for each target.

Let $x_i \in \mathbb{R}^d$ denote the ith input sample and y_i the corresponding target output. An XGBoost model composed of m trees is first trained, and for each sample it returns the terminal leaf index reached in each tree:

$$\ell_i = T_{\text{leaf}}(x_i) \in \mathbb{Z}^m, \tag{3}$$

where $\ell_i = [\ell_{i,1}, \ldots, \ell_{i,m}]$ encodes the decision-path locations across the ensemble. These discrete indices are transformed into a sparse binary vector using one-hot encoding:

$$z_i^{(\text{leaf})} = \text{OneHot}(\ell_i) \in \mathbb{R}^q, \tag{4}$$

where q denotes the total number of unique leaves across all m trees (after one-hot expansion). In parallel, an MLP is trained on the same

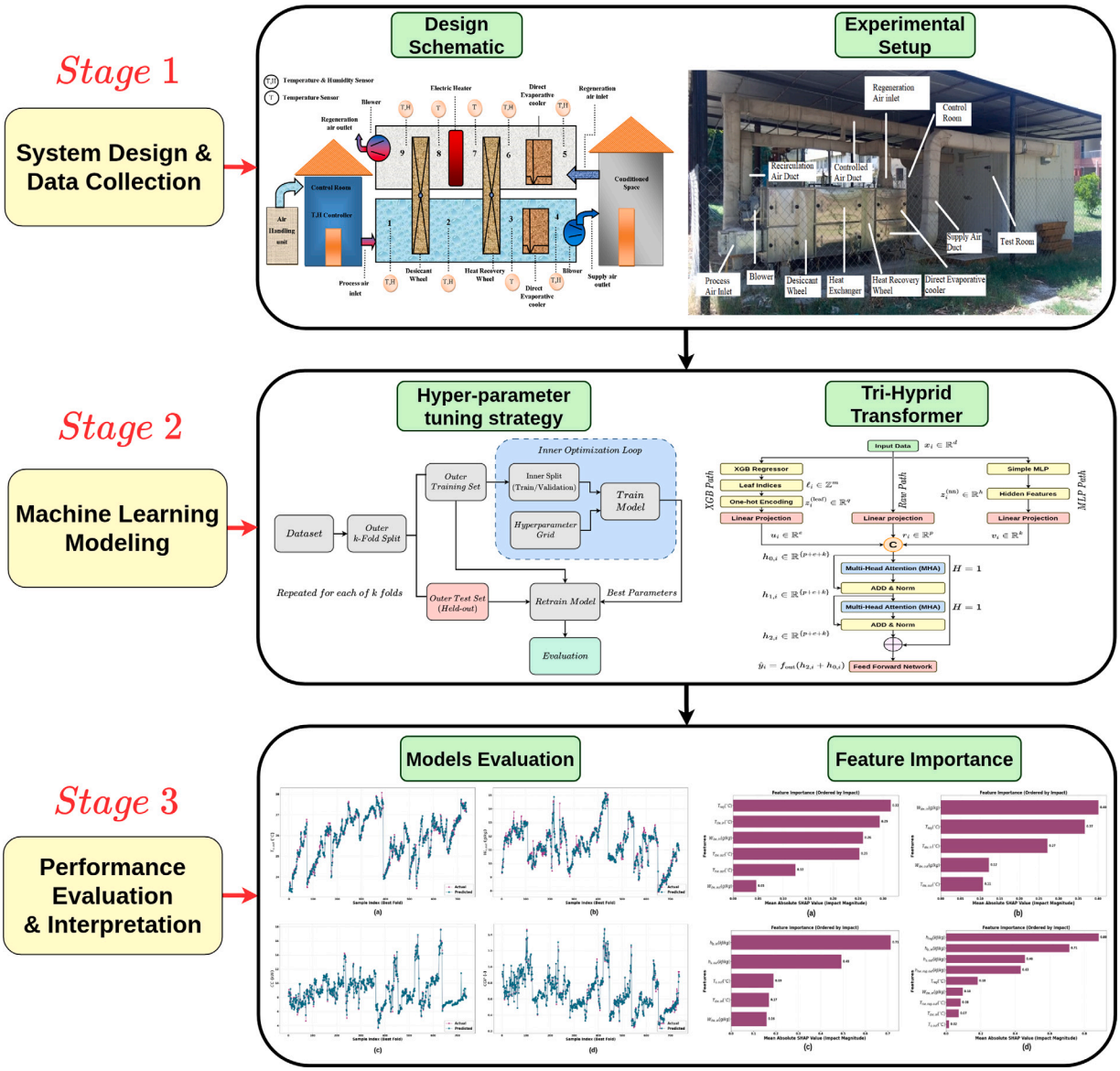


Fig. 3. Flowchart of the overall methodology showing the three main stages of the proposed framework.

Table 4
Summary of experimental cases, detailing input features, variable parameters, and target variables.

Case	Input features	Variable parameter	Range of variation	Target output
1	$T_{dw,in}, W_{dw,in}, T_{dw,out}, W_{dw,out}, T_{hw,out}, T_{reg}$	$T_{dw,in}$ T_{reg}	30–40 °C 60–90 °C	$T_{s,out}$
2	$T_{dw,in}, W_{dw,in}, T_{dw,out}, W_{dw,out}, T_{reg}$	$W_{dw,in}$ T_{reg}	12–20 g/kg 60–90 °C	$W_{s,out}$
3	$T_{dw,in}, W_{dw,in}, h_{p,in}, T_{s,out}, h_{s,out}$	$T_{dw,in}$ $W_{dw,in}$ T_{reg}	30–40 °C 12–20 g/kg 60–90 °C	CC
4	$T_{dw,in}, W_{dw,in}, h_{p,in}, T_{s,out}, h_{s,out}, T_{hw,reg,out}, h_{hw,reg,out}, T_{reg}, h_{reg}$	$T_{dw,in}$ $W_{dw,in}$ T_{reg}	30–40 °C 12–20 g/kg 60–90 °C	COP

inputs, and the activation of its final hidden layer is extracted as a neural embedding:

$$z_i^{(\mathrm{nn})} = \phi_{\mathrm{hid}}(x_i) \in \mathbb{R}^h, \tag{5}$$

where h is the dimensionality of the hidden feature vector. To fuse the raw inputs with tree- and neural-derived embeddings, each representation is projected into a learnable latent space and concatenated:

$$r_i = W_r x_i + b_r \in \mathbb{R}^p, \tag{6}$$

$$u_i = W_\ell z_i^{(\mathrm{leaf})} + b_\ell \in \mathbb{R}^e, \tag{7}$$

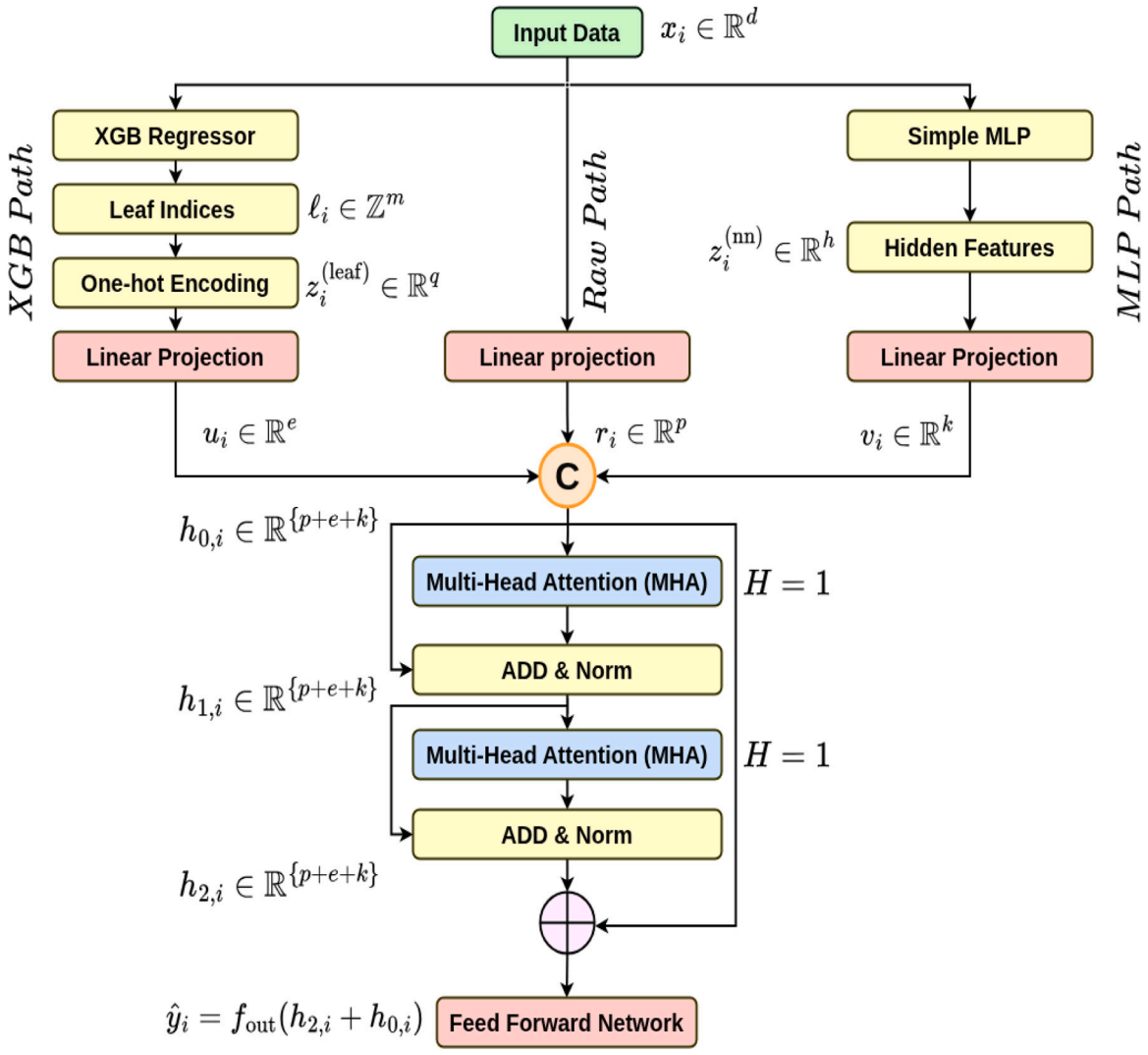


Fig. 4. Schematic architecture of the proposed Tri-Hybrid Transformer model.

$$v_i = W_n z_i^{(\text{nn})} + b_n \in \mathbb{R}^k, \tag{8}$$

$$h_{0,i} = [\, r_i \parallel u_i \parallel v_i \,] \in \mathbb{R}^{p+e+k}, \tag{9}$$

where p is the raw-input projection dimension, e is the tree-embedding projection dimension, and k is the neural-embedding projection dimension; W_r, W_ℓ, W_n and b_r, b_ℓ, b_n are trainable parameters, and $\parallel$ denotes concatenation. The fused representation $h_{0,i}$ is refined using two Transformer-style attention fusion blocks with residual connections and layer normalization [50,51]:

$$h_{1,i} = \mathrm{LN}\big(h_{0,i} + \mathrm{MHA}_1(h_{0,i})\big), \tag{10}$$

$$h_{2,i} = \mathrm{LN}\big(h_{1,i} + \mathrm{MHA}_2(h_{1,i})\big), \tag{11}$$

where MHA(·) denotes the self-attention mechanism (configured with a single head in this study) and LN(·) denotes layer normalization. A single attention head was adopted to prevent over-parameterization given the moderate dataset size and to focus on global feature interaction patterns rather than multi-head subspace decomposition. Residual connections preserve informative representations and improve optimization stability [52]. Finally, the regression output is produced by a feedforward output head:

$$\hat{y}_i = f_{\text{out}}\big(h_{2,i} + h_{0,i}\big), \tag{12}$$

where $f_{\text{out}}(\cdot)$ is a multilayer perceptron with nonlinear activation (e.g., ReLU). The residual fusion $(h_{2,i} + h_{0,i})$ ensures that both the original fused embedding and the attention-refined representation contribute to the final prediction.

3.4. Hyperparameter tuning strategy

To ensure a consistent and fair comparison across different operating conditions, the hyperparameter tuning procedure was standardized across all experiments and applied independently to each predictive model. In each case, model training was integrated within a cross-validation framework, and hyperparameters were selected based only on information available from the corresponding training subsets, ensuring no data leakage. This uniform tuning protocol guarantees that performance differences observed across experiments are attributable to variations in the underlying data rather than differences in optimization settings or validation methodologies. The tuning procedure was standardized across all models to ensure a fair comparison under identical validation, preprocessing, and evaluation conditions, thereby preventing optimization bias toward any specific algorithm.

For the classical machine learning models (Random Forest, SVR, and XGBoost), hyperparameters were optimized using an exhaustive grid search over predefined parameter spaces. In each outer cross-validation fold, the training data was used to perform an internal validation process (inner resampling or hold-out split, depending on the specific model). The best-performing configuration was identified, after

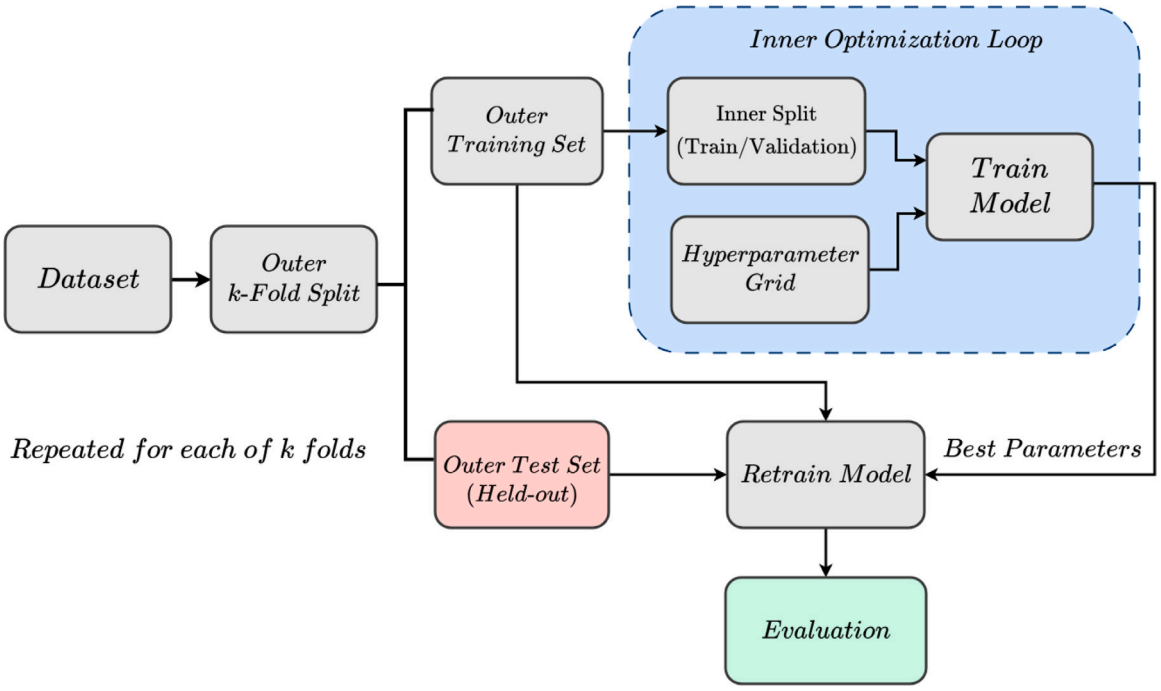


Fig. 5. Schematic representation of the standardized nested cross-validation framework used for hyperparameter tuning. The procedure separates the *inner optimization loop*, where hyperparameters are selected using only the outer training subset, from the *outer evaluation loop*, where the model is retrained and evaluated on the held-out test set.

which the model was retrained using the selected hyperparameters on the entire training fold and evaluated on the held-out test fold. This process was repeated across all folds, and the results from each fold were aggregated to produce reliable performance estimates.

For deep learning-based models (MLP and Tabular Transformer), a similar grid search strategy was employed, but using custom training loops instead of library-based `GridSearchCV`. Candidate configurations were manually trained for a fixed number of epochs, and the validation performance on the internal validation split was used to determine the optimal configuration for each fold. The final model was then retrained on the complete training set for that fold using the chosen hyperparameters before evaluating it on the test fold.

For the proposed Tri-Hybrid model, the tuning procedure adhered to the same principle of using training data only. Given the multi-stage architecture, the XGBoost and MLP components were trained with fixed hyperparameters to isolate the contribution of the fusion mechanism, while only the Transformer fusion module was tuned. Specifically, the learning rate and batch size of the fusion Transformer were optimized over a small grid using an internal split of the outer training data (inner validation). The selected Transformer setting was then held constant during the subsequent outer-fold training and evaluation for that fold, preserving the separation between hyperparameter selection and testing and preventing leakage. The full list of hyperparameters and their corresponding search spaces for each model evaluated is provided in Table 5, and the overall nested tuning workflow is illustrated in Fig. 5.

3.5. Evaluation metrics

To evaluate the predictive performance of the six regression models for the DECS's performance indicators, a comprehensive set of statistical error metrics was calculated using the actual, unscaled target values (y). These metrics were computed for each fold within the 5-fold cross-validation framework to ensure a robust assessment across different data partitions.

Mean Absolute Error (MAE), which measures the average absolute deviation between measured values (y_i) and model predictions ($\hat{y}_i$) over n samples, is defined as in Eq. (13):

$$\mathrm{MAE} = \frac{1}{n}\sum_{i=1}^{n}|y_i - \hat{y}_i| \tag{13}$$

Mean Squared Error (MSE), which computes the mean of squared residuals and therefore penalizes larger errors more strongly, is given by Eq. (14):

$$\mathrm{MSE} = \frac{1}{n}\sum_{i=1}^{n}(y_i - \hat{y}_i)^2 \tag{14}$$

Root Mean Squared Error (RMSE), obtained as the square root of MSE, provides an interpretable error measure in the same physical units as the target variable and is expressed in Eq. (15):

$$\mathrm{RMSE} = \sqrt{\frac{1}{n}\sum_{i=1}^{n}(y_i - \hat{y}_i)^2} \tag{15}$$

Coefficient of Determination (R^2), which quantifies the proportion of variance in the measured output explained by the model, ranges from $-\infty$ to 1 (perfect prediction). Negative values indicate performance worse than predicting the mean. It is computed as in Eq. (16):

$$R^2 = 1 - \frac{\sum_{i=1}^{n}(y_i - \hat{y}_i)^2}{\sum_{i=1}^{n}(y_i - \bar{y})^2}, \quad \text{where } \bar{y} = \frac{1}{n}\sum_{i=1}^{n} y_i \tag{16}$$

Adjusted R^2, which extends R^2 (Eq. (16)) by accounting for the number of predictors p and penalizing unnecessary model complexity, is defined as in Eq. (17):

$$\mathrm{Adj}\ R^2 = 1 - (1 - R^2)\cdot\frac{n-1}{n-p-1} \tag{17}$$

Mean Absolute Percentage Error (MAPE), which measures relative error in percentage form, is calculated as in Eq. (18). The small constant $\epsilon = 10^{-10}$ is used to prevent division by zero:

$$\mathrm{MAPE} = \frac{100}{n}\sum_{i=1}^{n}\frac{|y_i - \hat{y}_i|}{\epsilon + |y_i|} \tag{18}$$

Table 5
Hyperparameters and their search spaces for the models evaluated.

Model	Hyperparameter	Range of values
Random Forest (RF)	Number of Estimators (*n_estimators*)	[50, 100, 200, 300]
	Maximum Depth (*max_depth*)	[None, 10, 20, 50]
	Minimum Samples Split (*min_samples_split*)	[2, 5, 10]
	Minimum Samples Leaf (*min_samples_leaf*)	[1, 2, 4]
XGBoost	Number of Estimators (*n_estimators*)	[100, 300, 500]
	Maximum Depth (*max_depth*)	[3, 5, 7]
	Learning Rate (*learning_rate*)	[0.01, 0.05, 0.1]
	Subsample (*subsample*)	[0.7, 0.8, 1.0]
SVR	C (Regularization)	[0.1, 1, 10]
	Kernel Type	[Linear, RBF]
	Gamma (γ)	[scale, auto, 0.1, 1]
	Epsilon (ϵ)	[0.01, 0.1, 0.2]
MLP (ANN)	Hidden Layer Size (*hidden_dim*)	[64, 128, 256]
	Learning Rate (*learning_rate*)	[0.001, 0.01, 0.1]
	Number of Epochs (*epochs*)	[100, 150, 200]
Tabular Transformer	Embedding Dimension (*d_model*)	[32, 64]
	Number of Layers (*num_layers*)	[1, 2]
	Number of Attention Heads (*nhead*)	[2, 4]
	Learning Rate (*learning_rate*)	[0.001, 0.005]
	Batch Size (*batch_size*)	[16, 32]
Tri-Hybrid Transformer Model	Fusion Transformer Learning Rate (*learning_rate*)	[0.001, 0.005]
	Fusion Transformer Batch Size (*batch_size*)	[16, 32]

MAPE may become unstable when the true values approach zero ($y_i \approx 0$).

Median Absolute Error (MedAE), which provides an outlier-robust estimate of typical prediction error by taking the median absolute residual, is given in Eq. (19):

$$\mathrm{MedAE} = \mathrm{median}(|y_1 - \hat{y}_1|, \ldots, |y_n - \hat{y}_n|) \tag{19}$$

Explained Variance Score (EV), which measures the reduction in output variance achieved by the model and complements R^2 (Eq. (16)), is computed as in Eq. (20):

$$\mathrm{EV} = 1 - \frac{\mathrm{Var}(y - \hat{y})}{\mathrm{Var}(y)} \tag{20}$$

Mean Bias Deviation (MBD), which detects systematic prediction bias (positive values indicate underestimation when using $y_i - \hat{y}_i$), is defined in Eq. (21):

$$\mathrm{MBD} = \frac{1}{n}\sum_{i=1}^{n}(y_i - \hat{y}_i) \tag{21}$$

Collectively, these metrics provide a detailed evaluation of model accuracy, robustness, variance explanation, and bias across different operating conditions and target performance indicators.

4. Results and discussion

The predictive performance of the proposed Tri-Hybrid Transformer framework is evaluated across four key indicators, $T_{s,out}$, $W_{s,out}$, CC, and COP. The analysis encompasses detailed cross-validation assessment, comprehensive benchmark comparison against five established algorithms, and SHAP-based interpretability to verify physical consistency of model predictions.

4.1. Performance of the tri-hybrid transformer model

The predictive performance of the proposed Tri-Hybrid Transformer was assessed across four experimental cases, covering both primary supply-air states and derived system-level performance indices. Following the nested cross-validation procedure described in Section 3.4, all metrics were computed on the *original (inverse-transformed)* target values to preserve physical units and enable direct comparison with measurements.

The strong performance observed across the experimental cases is consistent with the tri-hybrid design. The XGBoost branch contributes regime-aware structure through leaf encodings, capturing operating-condition-dependent partitions typical of adsorption–desorption and rotary heat exchange processes. In parallel, the MLP branch learns smooth continuous nonlinear thermodynamic trends. The Transformer fusion module then combines the raw inputs with these complementary representations via attention, enabling target-specific interaction learning and improving robustness—particularly for derived indices such as CC and COP, where single-paradigm predictors can suffer from accumulated error.

Fold-wise results and aggregated statistics (Mean, Standard Deviation, and Median) are reported in Table 6. Overall, the model shows strong agreement with experimental measurements in all cases, achieving $R^2 > 0.95$ with near-zero mean bias deviation (MBD), indicating accurate and largely unbiased predictions.

For supply air temperature ($T_{s,out}$), the model attains $R^2 = 0.983$, MAPE = 0.38%, and RMSE = 0.137 °C. This RMSE is comparable to the Pt-100 sensor uncertainty (±0.15 °C), suggesting that further improvements may be limited by measurement noise rather than model capacity. For supply humidity ratio ($W_{s,out}$), robust accuracy is maintained ($R^2 = 0.956$; RMSE = 0.285 g/kg) with negligible bias (MBD ≈ -0.005), despite the nonlinear adsorption dynamics of the silica-gel wheel.

For system-level indices, the model remains highly effective in capturing multivariate dependencies: cooling capacity (CC) is predicted with $R^2 = 0.988$ and MAPE = 1.08%, while coefficient of performance (COP) achieves $R^2 = 0.992$ with approximately zero bias (MBD ≈ 0). Finally, the low fold-to-fold variability (e.g., $\sigma_{R^2} = 0.003$ for COP) confirms that the reported performance is stable across data partitions. Since hyperparameter selection was separated from outer-fold testing within the nested framework, these results provide a reliable estimate of generalization under practical operating conditions.

To visually corroborate the statistical results in Table 6, Fig. 6 shows predicted versus measured values for the four targets. Unlike the fold-wise reporting in Table 6, each panel pools predictions from all cross-validation folds into a single dataset for the corresponding experiment. The plots include the ideal $y = x$ line, the fitted regression line, a $\pm 1\sigma$ residual band, and 90th-percentile error bounds.

Across all cases, the predictions exhibit strong linear agreement with the experimental measurements over the full operating range, as reflected by the tight clustering around the diagonal. For supply air

Table 6
Detailed performance metrics of the Tri-Hybrid Transformer model across the experimental cases. The table presents the individual results for each cross-validation fold, along with the aggregated Mean, Standard Deviation, and Median values.

Fold	MAE	MSE	RMSE	R^2	Adj. R^2	MAPE (%)	MedianAE	EV	MBD
Target Output: Supply Temp ($T_{s,out}$)									
Fold 1	0.099	0.020	0.140	0.984	0.984	0.38	0.073	0.984	0.009
Fold 2	0.093	0.017	0.130	0.984	0.984	0.36	0.066	0.985	−0.009
Fold 3	0.100	0.019	0.140	0.982	0.982	0.39	0.072	0.982	−0.010
Fold 4	0.099	0.019	0.139	0.983	0.983	0.39	0.072	0.983	−0.003
Fold 5	0.100	0.019	0.139	0.983	0.983	0.39	0.070	0.983	0.000
Mean	0.098	0.019	0.137	0.983	0.983	0.38	0.071	0.983	−0.003
Std Dev	0.003	0.001	0.004	0.001	0.001	0.01	0.003	0.001	0.008
Median	0.099	0.019	0.139	0.983	0.983	0.39	0.072	0.983	−0.003
Target Output: Supply Humidity ($W_{s,out}$)									
Fold 1	0.187	0.087	0.295	0.955	0.955	1.68	0.115	0.955	0.005
Fold 2	0.183	0.087	0.294	0.954	0.954	1.65	0.123	0.954	−0.017
Fold 3	0.177	0.073	0.270	0.960	0.960	1.57	0.124	0.961	0.012
Fold 4	0.176	0.080	0.282	0.957	0.957	1.54	0.117	0.958	−0.028
Fold 5	0.177	0.079	0.280	0.951	0.951	1.57	0.119	0.951	0.004
Mean	0.180	0.081	0.285	0.956	0.955	1.60	0.119	0.956	−0.005
Std Dev	0.005	0.006	0.010	0.003	0.003	0.06	0.004	0.004	0.017
Median	0.177	0.080	0.282	0.955	0.955	1.57	0.119	0.955	0.004
Target Output: Cooling Capacity (CC)									
Fold 1	0.082	0.035	0.187	0.992	0.992	1.00	0.047	0.992	−0.012
Fold 2	0.093	0.046	0.213	0.991	0.990	1.06	0.057	0.991	0.001
Fold 3	0.097	0.085	0.292	0.981	0.981	1.17	0.056	0.981	−0.005
Fold 4	0.089	0.051	0.227	0.989	0.989	1.04	0.054	0.989	−0.013
Fold 5	0.095	0.050	0.224	0.990	0.990	1.11	0.063	0.990	−0.019
Mean	0.091	0.053	0.229	0.988	0.988	1.08	0.055	0.988	−0.010
Std Dev	0.006	0.019	0.039	0.004	0.004	0.06	0.006	0.004	0.008
Median	0.093	0.050	0.224	0.990	0.990	1.06	0.056	0.990	−0.012
Target Output: Coeff. of Perf. (COP)									
Fold 1	0.008	0.000	0.017	0.993	0.993	1.32	0.004	0.993	0.001
Fold 2	0.010	0.001	0.023	0.989	0.988	1.61	0.005	0.989	0.004
Fold 3	0.008	0.000	0.017	0.994	0.994	1.43	0.004	0.994	−0.002
Fold 4	0.009	0.000	0.017	0.994	0.994	1.51	0.005	0.994	−0.002
Fold 5	0.009	0.000	0.021	0.988	0.988	1.52	0.004	0.989	−0.001
Mean	0.009	0.000	0.019	0.992	0.992	1.48	0.004	0.992	−5.4e−05
Std Dev	0.001	0.000	0.003	0.003	0.003	0.11	0.001	0.003	0.003
Median	0.009	0.000	0.017	0.993	0.993	1.51	0.004	0.993	−0.001

temperature (Fig. 6(a)), the fitted relation ($y = 0.98x + 0.47$) has a slope close to unity and a small intercept, indicating minimal global bias. A similar behavior is observed for supply humidity ratio (Fig. 6(b)), where the fitted line ($y = 0.95x + 0.55$) deviates only slightly from the ideal mapping. Although this case shows a modest increase in dispersion — consistent with the higher nonlinearity of moisture-transfer dynamics — the spread remains balanced without systematic variance inflation at higher humidity levels.

For cooling capacity (Fig. 6(c)), the model tracks system load robustly, with most points contained within the $\pm 1\sigma$ band and a fitted relation close to ideal ($y = 0.98x + 0.19$). The coefficient of performance (Fig. 6(d)) shows the tightest alignment overall, with very limited outlier behavior and an almost unbiased fit ($y = 0.9x + 0.01$). Overall, the concentration of samples within the 90th-percentile bounds across all panels supports the stability of the model and its ability to generalize across operating conditions.

To complement the pooled regression analysis in Fig. 6 and provide an intuitive view of pointwise tracking, Fig. 7 presents the predicted and measured outputs for the best-performing fold of each experiment. The results are plotted versus sample index for (a) $T_{s,out}$, (b) $W_{s,out}$, (c) CC, and (d) COP. Across all four cases, the Tri-Hybrid model follows the measured trajectories closely, capturing both smooth trends and abrupt regime transitions that arise under changing operating conditions. The largest deviations are primarily localized around sharp transients, where rapid dynamics and measurement noise can dominate. These best-fold curves are included as qualitative evidence of tracking fidelity; the quantitative conclusions are based on the aggregated cross-validation statistics reported in Table 6.

4.2. Comparison with benchmark models

The predictive capabilities of the proposed Tri-Hybrid Transformer were rigorously benchmarked against five established regression algorithms: XGBoost, Support Vector Regression (SVR), Random Forest (RF), a feedforward neural network (MLP), and a Tabular Transformer. The quantitative comparison across the four target variables ($T_{s,out}$, $W_{s,out}$, CC, and COP) is summarized in Table 7, where metrics are reported as Mean ± Standard Deviation over the cross-validation folds.

To facilitate a unified multi-objective assessment, Fig. 8 presents a radar chart comparison of the model footprints. It is important to note that all axes in Fig. 8 have been normalized and oriented such that the origin (center) represents the ideal performance. Specifically, the error and bias metrics (MAE, MSE, RMSE, MAPE, MedianAE, and MBD) are normalized relative to the maximum observed error across the models. Conversely, the goodness-of-fit metrics (R^2, Adj. R^2, and EV) are inverted (calculated as $1 - \text{metric}$) so that the ideal value of 1 maps to the chart origin. Consequently, a smaller polygon area concentrated near the center signifies superior overall robustness, whereas outward expansions indicate performance degradation.

As shown in Table 7, the Tri-Hybrid model achieves the most consistent overall performance. For supply-air temperature $T_{s,out}$, it attains the lowest RMSE (0.1375) and the highest R^2 (0.9834). While tree ensembles (RF and XGBoost) remain competitive for this relatively smooth target, their performance advantage does not transfer uniformly to the remaining cases. This trend is clearly reflected in Fig. 8(a), where the proposed model (red polygon) maintains the tightest cluster around

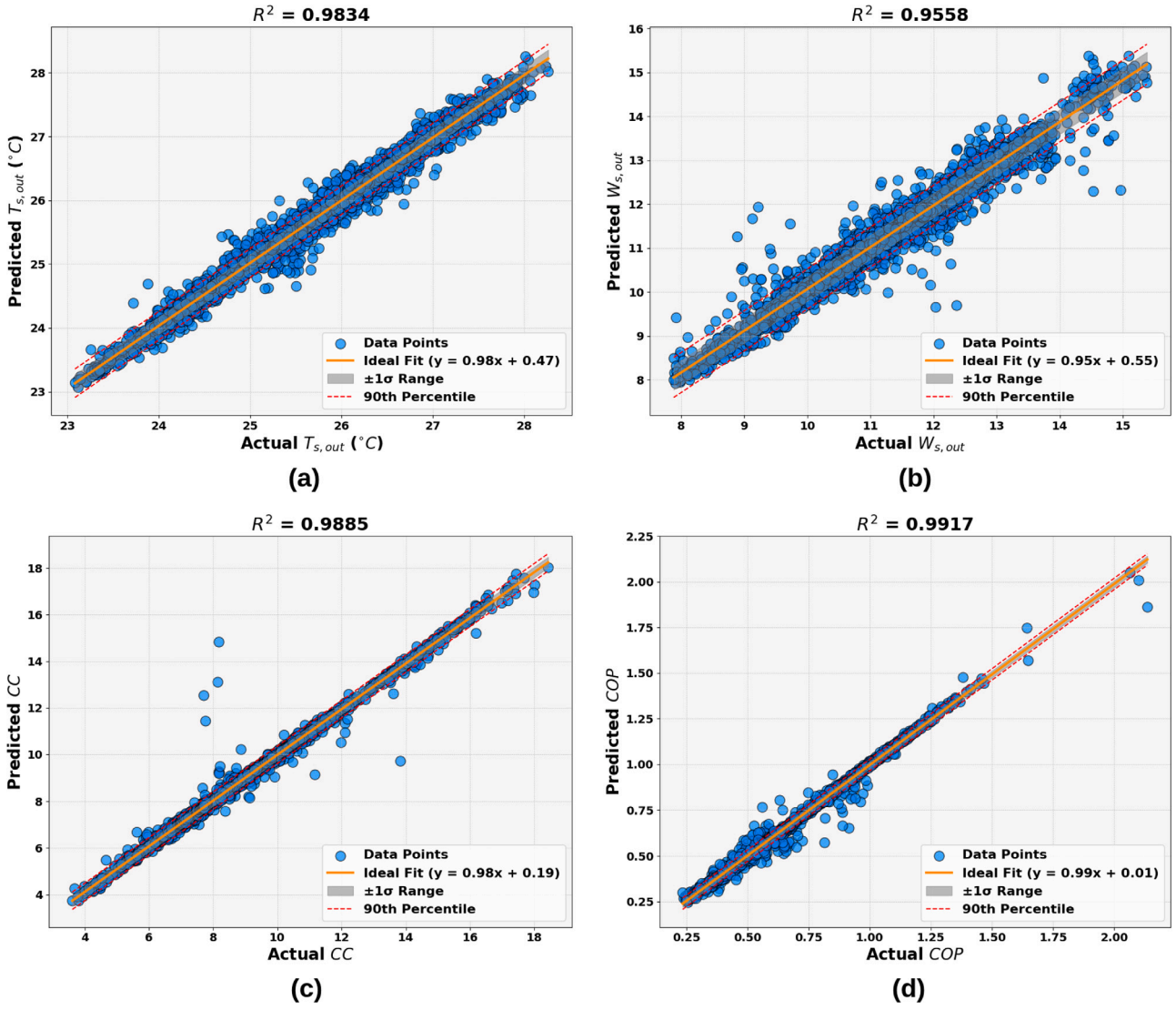


Fig. 6. Regression plots pooling predictions from all cross-validation folds. Panels show predicted vs. measured values for (a) $T_{s,out}$, (b) $W_{s,out}$, (c) CC, and (d) COP. The plots include the ideal $y = x$ line, the fitted regression line, a $\pm 1\sigma$ residual band, and 90th-percentile error bounds.

the origin across all axes, indicating a balanced reduction in both bias and variance.

The superiority of the fusion approach becomes clearer for humidity prediction $W_{s,out}$, which is governed by nonlinear adsorption dynamics. Table 7 shows that the Tri-Hybrid model yields the highest R^2 (0.9556) with the lowest MAE (0.1801), whereas XGBoost and SVR degrade substantially ($R^2 < 0.88$). Fig. 8(b) visually captures this disparity; the baselines exhibit large spikes along the error axes (outer edge), while the proposed model retains its compact, central shape.

For the system-level metrics CC and COP, the advantage of the Tri-Hybrid design is even more pronounced. Cooling capacity is predicted with the best overall fit ($R^2 = 0.9884$) and the lowest MAPE (1.08%). In contrast, XGBoost becomes unstable for this variable, a failure mode visible in Fig. 8(c) as a sharp expansion along the MAPE and MSE axes. Similarly, for COP, the Tri-Hybrid model achieves the best global accuracy. Although SVR attains the smallest MedAE, its advantage is local; the proposed model exhibits a more balanced reduction across the full set of metrics, occupying the most favorable (central) region in Fig. 8(d).

Overall, the results confirm that the proposed Tri-Hybrid architecture — by fusing regime-aware encodings with continuous latent representations — mitigates the trade-offs typical of single-paradigm models, yielding a predictor that is not only accurate but consistently robust across diverse thermodynamic regimes.

To provide deeper insight into predictive fidelity beyond the scalar error metrics, Taylor diagrams are shown in Fig. 9. This compact visualization summarizes three complementary statistics simultaneously: the Pearson correlation coefficient (R, given by the azimuthal angle), the standard deviation of the predictions (σ, given by the radial distance), and the centered root-mean-square difference (RMSD, given by the distance to the reference point). The observed dataset is represented by the black marker on the x-axis; an ideal model would coincide with this reference, indicating perfect correlation, matched variability, and zero centered RMSD.

As seen in Fig. 9(a)–Fig. 9(d), the proposed Tri-Hybrid model consistently lies closest to the observation reference compared with the benchmark predictors. For supply temperature, Fig. 9(a) shows that the Tri-Hybrid model achieves a high correlation ($R \approx 0.98$) while reproducing the measured variability (i.e., σ closely matches the observed standard deviation). In contrast, SVR is displaced from the reference arc, reflecting reduced correlation and a mismatch in variance, which is consistent with its larger errors reported in Table 7.

The advantage becomes clearer for the more complex system-level indicator, cooling capacity. In Fig. 9(c), the Tri-Hybrid model clusters

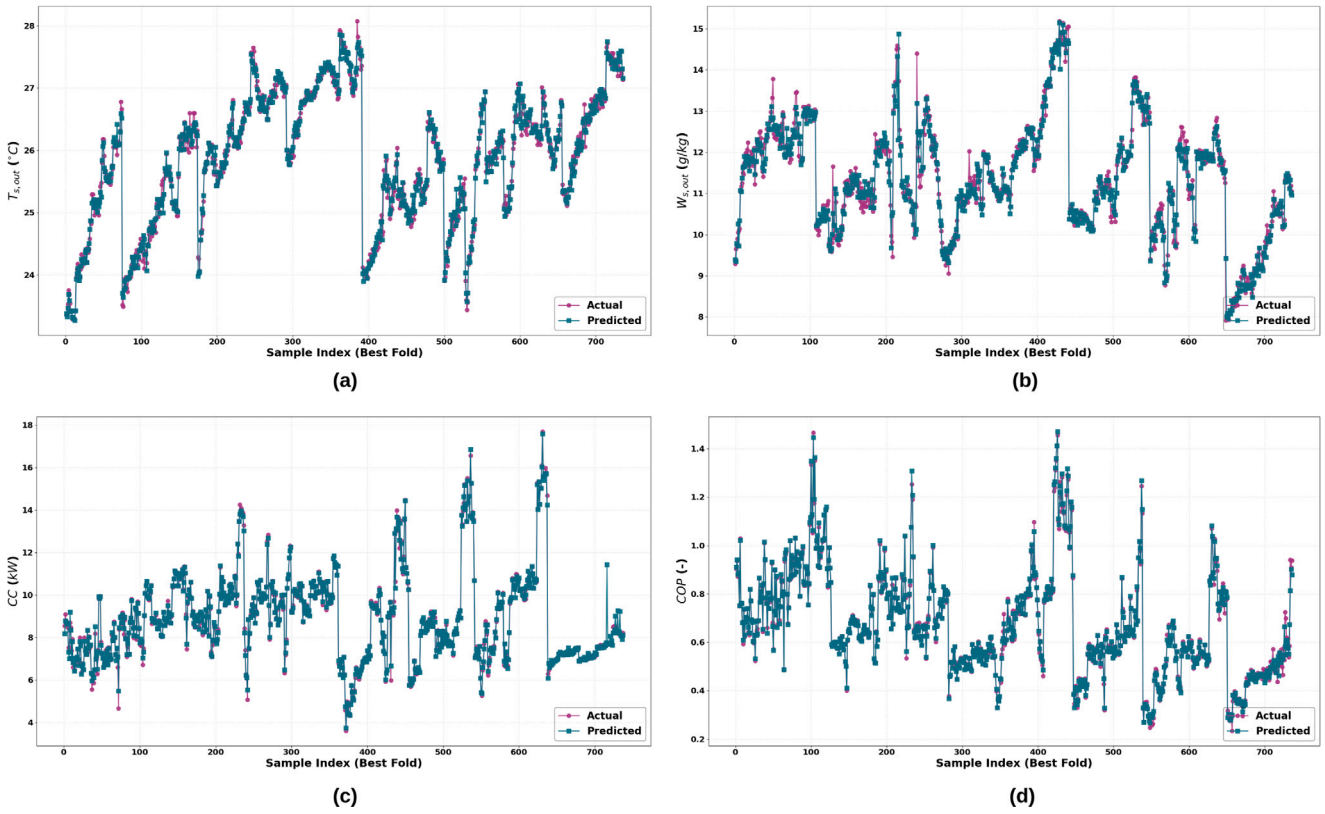


Fig. 7. Best-fold tracking plots of the Tri-Hybrid Transformer model for the four target variables: (a) supply air temperature $T_{s,out}$, (b) supply humidity ratio $W_{s,out}$, (c) cooling capacity CC, and (d) coefficient of performance COP. Predicted and measured values are shown versus sample index within the best-performing fold (selected by test-fold R^2) to provide a representative visualization of pointwise agreement.

near the reference point, indicating that it captures both the amplitude of variability and the overall pattern of CC without significant distortion. By comparison, XGBoost and Random Forest show noticeable radial offsets, suggesting difficulty in matching the full variance of the cooling-capacity signal across operating regimes, which aligns with their weaker and less stable performance in Table 7 and the broader footprints in Fig. 8.

Overall, the Taylor-diagram assessment reinforces the comparative conclusions drawn from Table 7 and Fig. 8: the proposed Tri-Hybrid model achieves a consistently favorable balance of high correlation (reduced pattern error) and well-preserved standard deviation (correct variability), leading to the smallest centered RMSD across the evaluated thermodynamic targets.

To assess the practical reliability of the proposed DECS framework, the experimentally obtained system performance was benchmarked against representative desiccant evaporative cooling studies with comparable operating configurations and performance indicators. Table 8 presents a comparative summary based on research methodology, system configuration, and reported COP.

The comparison demonstrates that the performance achieved in the current study remains within the range reported for similar solar-assisted and hybrid desiccant evaporative cooling systems. In particular, the obtained COP range of 0.4–2.1 shows good agreement with experimentally validated and simulation-based investigations conducted under different climatic and operating conditions.

Overall, the comparative assessment confirms that the proposed DECS framework achieves thermodynamically competitive performance while maintaining consistency with previously reported system-level results. This agreement further supports the reliability of the experimental setup, operating methodology, and overall system behavior presented in the current study.

4.3. Feature importance

To analyze the impact of different input variables on the Tri-Hybrid Transformer predictions, SHAP (SHapley Additive exPlanations) analysis was conducted. Fig. 10 summarizes the global feature importance for the four evaluated targets, where the bar length represents the mean absolute SHAP value, measuring the average magnitude of a feature's contribution to the model output across all samples.

Fig. 10(a) shows that the feature regeneration temperature (T_{reg}) with a significant SHAP value of 0.32 has a stronger influence on the targeted supply air temperature ($T_{s,out}$). It is because at higher regeneration temperature, the dehumidification capacity of the desiccant wheel is increased. When this highly dry air passes through the direct evaporative cooler (DEC), the evaporation is enhanced, which reduces the supply air temperature to the desired thermal comfort level. In the DEC, $T_{s,out}$ is more responsive to latent cooling potential as compared to sensible cooling. Additionally, T_{reg} mainly controls the moisture removal and latent heat transfer, hence it occurs as the most influential parameter that directly affects $T_{s,out}$. In Fig. 10(b) the SHAP-based global feature importance shows that the process inlet air absolute humidity ($W_{dw,in}$) is the most dominant parameter governing the prediction of the supply air absolute humidity ($W_{s,out}$). This dominance occurs because of the moisture transfer mechanism during the dehumidification process in the desiccant wheel; where the moisture adsorption rate is mainly driven by the humidity potential difference between the desiccant material and the incoming process air stream. The higher process inlet air absolute humidity directly enhances the moisture removal potential, which in turn leads to substantial variation in the supply air absolute humidity.

Similarly, Fig. 10(c) shows that the process air inlet enthalpy ($h_{p,in}$) is the most dominating parameter that directly affects the cooling capacity (CC) of the system, followed by the supply air enthalpy

Table 7
Comprehensive comparison of model performance across four experimental cases. Rows represent statistical metrics, and columns represent the different models. Values are reported as Mean ± Standard Deviation. Best results per row are highlighted in bold. For MBD, the best value is the one with the smallest absolute mean bias, $|MBD|$.

Metric	XGBoost	SVR	Random Forest	MLP	Transformer	Tri-Hybrid (Proposed)
Target Output: Supply Temp ($T_{s,out}$)						
MAE	0.1103 ± 0.0049	0.1760 ± 0.0073	0.1117 ± 0.0052	0.1257 ± 0.0030	0.1269 ± 0.0093	**0.0982 ± 0.0029**
MSE	0.0241 ± 0.0019	0.0579 ± 0.0065	0.0269 ± 0.0029	0.0291 ± 0.0017	0.0294 ± 0.0046	**0.0189 ± 0.0012**
RMSE	0.1552 ± 0.0060	0.2403 ± 0.0141	0.1639 ± 0.0088	0.1704 ± 0.0049	0.1711 ± 0.0132	**0.1375 ± 0.0043**
R^2	0.9788 ± 0.0017	0.9492 ± 0.0047	0.9763 ± 0.0024	0.9744 ± 0.0022	0.9742 ± 0.0037	**0.9834 ± 0.0008**
Adj. R^2	0.9786 ± 0.0018	0.9487 ± 0.0048	0.9761 ± 0.0024	0.9742 ± 0.0022	0.9740 ± 0.0037	**0.9832 ± 0.0008**
MAPE (%)	0.4288 ± 0.0187	0.6820 ± 0.0289	0.4343 ± 0.0207	0.4872 ± 0.0117	0.4927 ± 0.0383	**0.3809 ± 0.0116**
MedAE	0.0814 ± 0.0048	0.1342 ± 0.0142	0.0773 ± 0.0061	0.0964 ± 0.0052	0.0978 ± 0.0096	**0.0707 ± 0.0031**
EV	0.9788 ± 0.0018	0.9493 ± 0.0047	0.9764 ± 0.0024	0.9745 ± 0.0022	0.9745 ± 0.0039	**0.9834 ± 0.0008**
MBD	−0.0011 ± 0.0054	0.0073 ± 0.0136	0.0016 ± 0.0077	**−0.0000 ± 0.0101**	0.0020 ± 0.0216	−0.0025 ± 0.0076
Target Output: Supply Humidity ($W_{s,out}$)						
MAE	0.3394 ± 0.0235	0.3311 ± 0.0120	0.1935 ± 0.0093	0.2173 ± 0.0171	0.2148 ± 0.0113	**0.1801 ± 0.0050**
MSE	0.2290 ± 0.0305	0.2411 ± 0.0258	0.0979 ± 0.0113	0.1050 ± 0.0191	0.1021 ± 0.0067	**0.0810 ± 0.0059**
RMSE	0.4777 ± 0.0320	0.4905 ± 0.0265	0.3125 ± 0.0175	0.3229 ± 0.0298	0.3194 ± 0.0106	**0.2845 ± 0.0104**
R^2	0.8745 ± 0.0174	0.8680 ± 0.0133	0.9464 ± 0.0058	0.9426 ± 0.0099	0.9439 ± 0.0055	**0.9556 ± 0.0035**
Adj. R^2	0.8736 ± 0.0175	0.8671 ± 0.0134	0.9460 ± 0.0058	0.9422 ± 0.0100	0.9436 ± 0.0055	**0.9553 ± 0.0035**
MAPE (%)	3.0527 ± 0.2167	2.9777 ± 0.1162	1.7219 ± 0.0855	1.9269 ± 0.1563	1.9117 ± 0.1164	**1.6029 ± 0.0603**
MedAE	0.2393 ± 0.0258	0.2230 ± 0.0151	**0.1151 ± 0.0084**	0.1511 ± 0.0148	0.1502 ± 0.0146	0.1193 ± 0.0040
EV	0.8748 ± 0.0171	0.8683 ± 0.0132	0.9464 ± 0.0057	0.9436 ± 0.0098	0.9447 ± 0.0045	**0.9557 ± 0.0035**
MBD	0.0004 ± 0.0291	−0.0114 ± 0.0252	**−0.0002 ± 0.0114**	0.0172 ± 0.0422	0.0183 ± 0.0339	−0.0049 ± 0.0166
Target Output: Cooling Capacity (CC)						
MAE	0.8702 ± 0.2298	0.1139 ± 0.0077	0.2240 ± 0.0305	0.1619 ± 0.0285	0.1795 ± 0.0341	**0.0910 ± 0.0058**
MSE	1.2651 ± 0.4691	0.1016 ± 0.0271	0.1839 ± 0.0174	0.0828 ± 0.0276	0.0936 ± 0.0314	**0.0534 ± 0.0190**
RMSE	1.1023 ± 0.2501	0.3166 ± 0.0411	0.4284 ± 0.0202	0.2847 ± 0.0464	0.3019 ± 0.0556	**0.2285 ± 0.0388**
R^2	0.7294 ± 0.0973	0.9779 ± 0.0068	0.9603 ± 0.0046	0.9820 ± 0.0065	0.9796 ± 0.0074	**0.9884 ± 0.0045**
Adj. R^2	0.7275 ± 0.0980	0.9778 ± 0.0068	0.9601 ± 0.0046	0.9819 ± 0.0066	0.9795 ± 0.0074	**0.9883 ± 0.0045**
MAPE (%)	10.1978 ± 2.6999	1.2798 ± 0.1137	2.6052 ± 0.3715	1.9101 ± 0.3258	2.1352 ± 0.4049	**1.0784 ± 0.0641**
MedAE	0.7648 ± 0.2327	**0.0274 ± 0.0015**	0.1327 ± 0.0360	0.1065 ± 0.0215	0.1248 ± 0.0370	0.0554 ± 0.0057
EV	0.7297 ± 0.0974	0.9780 ± 0.0067	0.9604 ± 0.0045	0.9823 ± 0.0066	0.9806 ± 0.0064	**0.9885 ± 0.0045**
MBD	**−0.0021 ± 0.0448**	−0.0101 ± 0.0154	−0.0071 ± 0.0176	−0.0238 ± 0.0291	0.0056 ± 0.0733	−0.0095 ± 0.0080
Target Output: Coeff. of Perf. (COP)						
MAE	0.0228 ± 0.0012	**0.0062 ± 0.0007**	0.0269 ± 0.0012	0.0121 ± 0.0024	0.0145 ± 0.0035	0.0087 ± 0.0008
MSE	0.0011 ± 0.0001	0.0004 ± 0.0001	0.0018 ± 0.0003	0.0005 ± 0.0002	0.0006 ± 0.0002	**0.0004 ± 0.0001**
RMSE	0.0334 ± 0.0019	0.0195 ± 0.0025	0.0423 ± 0.0041	0.0213 ± 0.0035	0.0239 ± 0.0049	**0.0189 ± 0.0028**
R^2	0.9743 ± 0.0026	0.9911 ± 0.0024	0.9588 ± 0.0061	0.9892 ± 0.0046	0.9863 ± 0.0060	**0.9916 ± 0.0028**
Adj. R^2	0.9740 ± 0.0027	0.9910 ± 0.0024	0.9583 ± 0.0062	0.9890 ± 0.0047	0.9862 ± 0.0061	**0.9915 ± 0.0029**
MAPE (%)	3.6045 ± 0.1836	**1.1112 ± 0.1250**	4.1381 ± 0.1884	2.1115 ± 0.4711	2.3018 ± 0.5202	1.4801 ± 0.1081
MedAE	0.0159 ± 0.0010	**0.0016 ± 0.0001**	0.0174 ± 0.0013	0.0085 ± 0.0029	0.0096 ± 0.0038	0.0043 ± 0.0005
EV	0.9744 ± 0.0026	0.9911 ± 0.0024	0.9588 ± 0.0061	0.9904 ± 0.0034	0.9872 ± 0.0057	**0.9917 ± 0.0027**
MBD	0.0003 ± 0.0017	0.0005 ± 0.0004	−0.0002 ± 0.0016	0.0061 ± 0.0037	0.0041 ± 0.0051	**−0.0001 ± 0.0026**

Table 8
Validation of the current DECS performance results against previously published literature.

Reference/Year	Type of research	System type	COP
Current Study/2026	Experimental + Machine Learning	Solar-DAC integrated direct evaporative cooling	0.4–2.1
[53]/2021	Experimental	Solar-DAC integrated direct evaporative cooling	0.35–0.6
[54]/2020	Experimental	Solar-DAC integrated direct evaporative cooling	2.1
[55]/2022	Simulation	Solar-DAC integrated direct evaporative cooling	0.89
[56]/2020	Numerical	DAC integrated direct evaporative cooling	1.89
[57]/2021	Experimental + Numerical	Solar-DAC integrated evaporative cooling	0.76

($h_{s,out}$). Since CC is primarily governed by the enthalpy difference between the process inlet and supply outlet air streams, including both sensible and latent heat components. The process air inlet enthalpy describes the overall thermal load imposed on the system, and changes in this parameter directly affect the variations in the achievable cooling output. The supply air outlet enthalpy represents the effectiveness of moisture and heat removal processes and therefore highly influences the net amount of cooling delivered. Moreover, Fig. 10(d) highlights that the regeneration air enthalpy (h_{reg}) is the most influential parameter that affects the COP of the system. The COP is defined as the ratio between the cooling output and the required thermal energy input. As desiccant-based air conditioning systems are mainly dependent on the regeneration energy, variations in regeneration air enthalpy have an inverse impact on the overall efficiency of the system. The results illustrate that COP of the system is primarily affected by regeneration energy requirements rather than process-side air conditions.

Overall, the SHAP results confirm that the Tri-Hybrid Transformer emphasizes variables with clear thermodynamic relevance — regeneration temperature for adsorption-driven behavior and enthalpy states for energy-based performance indices — supporting both the predictive reliability and interpretability of the proposed framework.

Detailed experimental investigations were conducted to evaluate the DECS performance under varying ambient conditions and operating scenarios. The system was tested under multiple combinations of process inlet temperature, inlet humidity ratio, and regeneration temperature to identify the optimal operating conditions and corresponding performance limits.

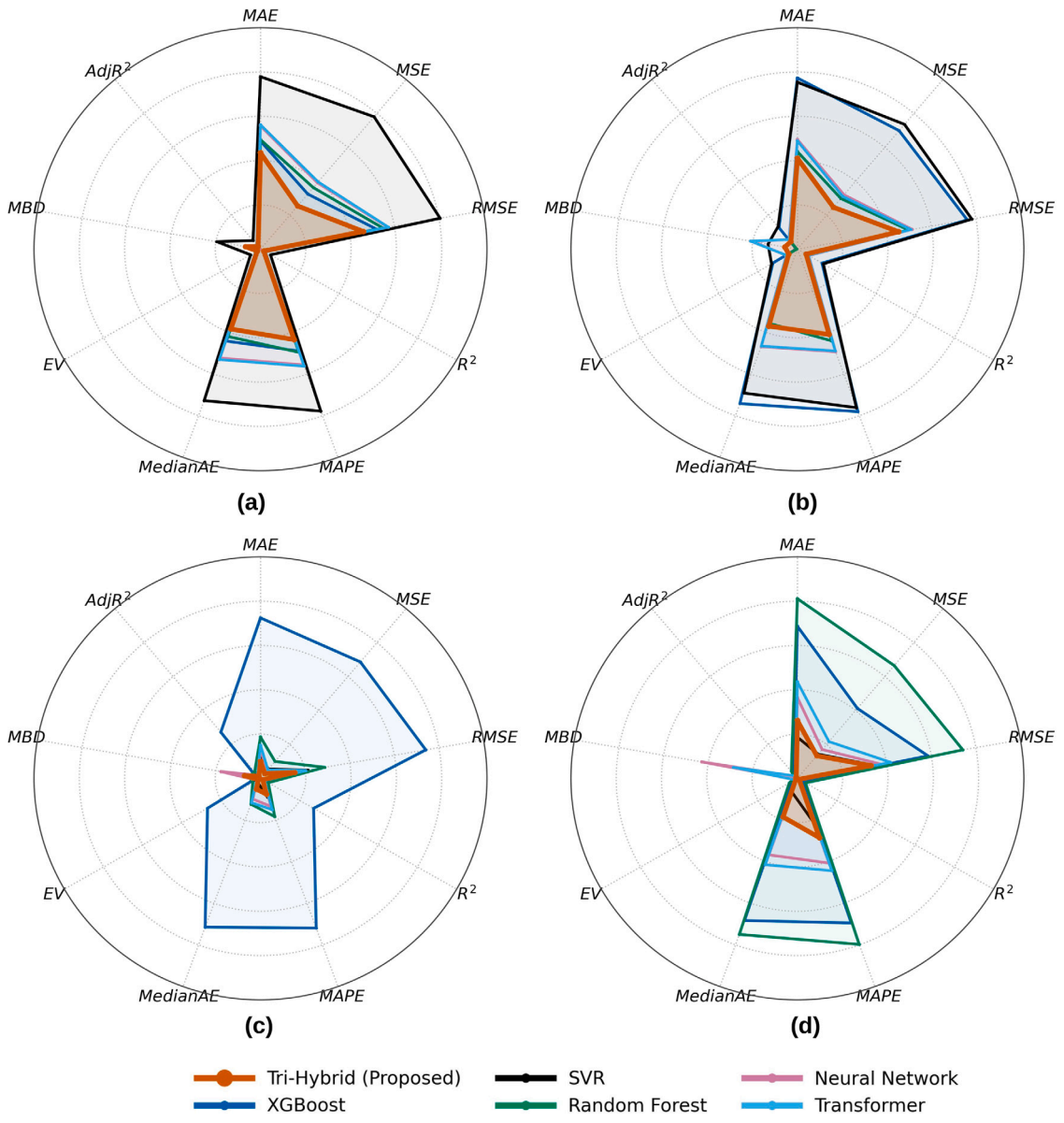


Fig. 8. Radar-chart comparison of the evaluated models across nine performance metrics for (a) $T_{s,out}$, (b) $W_{s,out}$, (c) CC, and (d) COP. The center of the chart represents ideal performance (zero error, unit R^2). Smaller, more central footprints indicate superior overall robustness.

The maximum thermal coefficient of performance (COP) achieved during the experiments was 2.1, obtained at a process inlet temperature of 38.2 °C, inlet humidity ratio of 13.92 g/kg, and regeneration temperature of 60.2 °C. When the process inlet temperature varied between 30–40 °C at a constant inlet humidity ratio of 14 g/kg and regeneration temperatures between 60–80 °C, the system COP ranged from 0.31 to 2.1.

In contrast, when the process inlet temperature was maintained at 30 °C and the inlet humidity ratio varied between 12–20 g/kg under regeneration temperatures ranging from 60–90 °C, the COP ranged between 0.23 and 1.46. The experimental analysis further revealed that the system COP generally increased with increasing process inlet temperature, whereas higher inlet humidity ratios reduced the overall system performance due to the increased latent cooling load. These findings provide a clearer understanding of the operational limits, optimal conditions, and thermodynamic behavior of the proposed DECS framework.

5. Conclusions

This study introduced a Tri-Hybrid Transformer framework for multi-target performance prediction of solid desiccant evaporative cooling system (DECS), addressing four critical gaps identified in the literature: restricted prediction scope, single-paradigm modeling limitations, inadequate generalization validation, and lack of interpretability. The framework's effectiveness was validated through comprehensive experimental testing and rigorous benchmarking against five established machine learning algorithms.

The proposed architecture achieved exceptional predictive accuracy across four thermodynamic outputs, with R^2 values of 0.983 for supply air temperature, 0.956 for supply humidity ratio, 0.988 for cooling capacity, and 0.992 for coefficient of performance. The RMSE of 0.137 °C for supply temperature approaches the Pt-100 sensor uncertainty (±0.15 °C), suggesting that further improvements may be limited by measurement noise rather than model capacity. This multi-target capability, developed through target-optimized input features acknowledging the distinct physics governing each output, represents

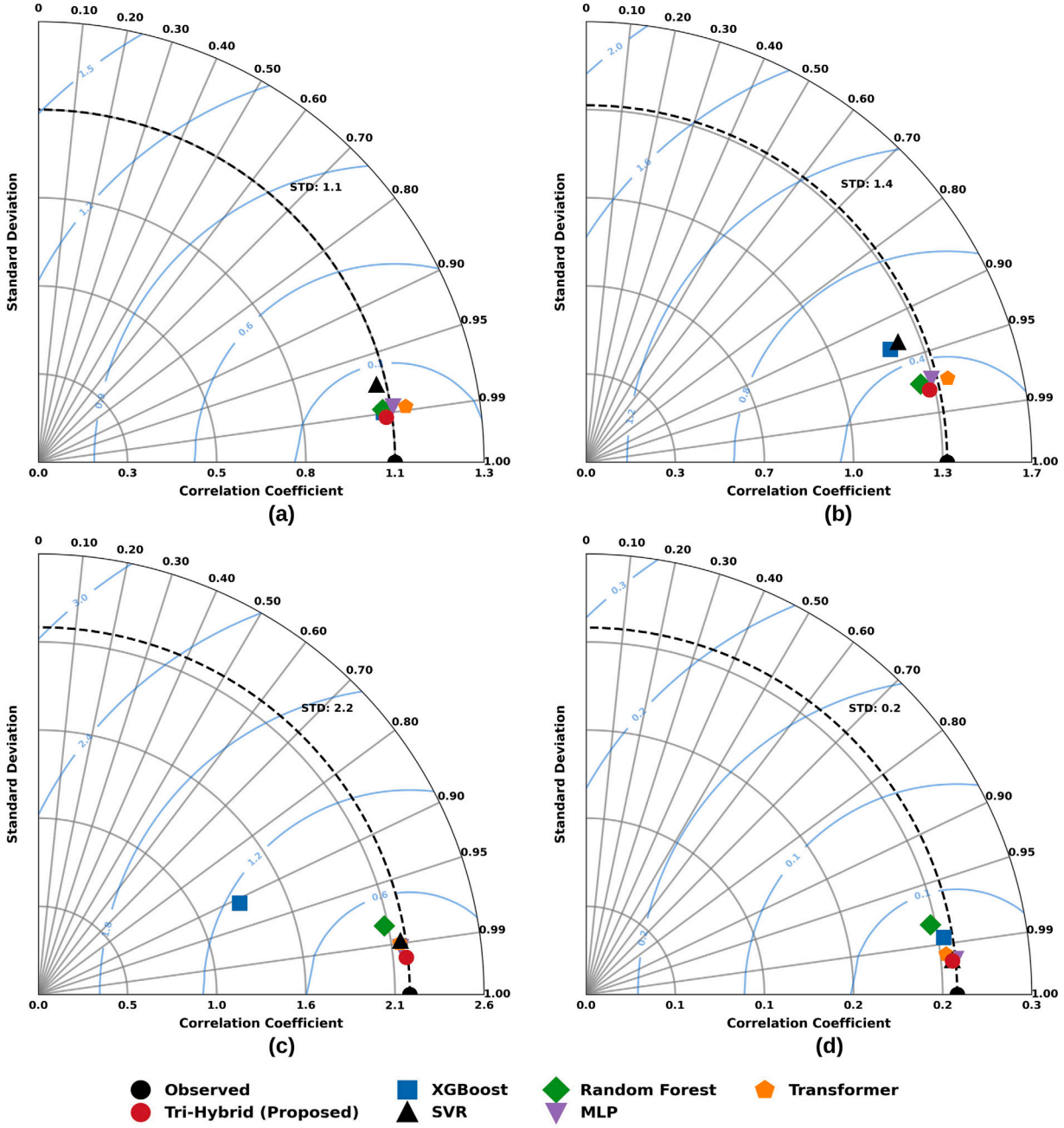


Fig. 9. Taylor diagrams illustrating the statistical fidelity of the predictions for (a) $T_{s,out}$, (b) $W_{s,out}$, (c) CC, and (d) COP. The radial distance represents the standard deviation (σ), and the angular position represents the correlation coefficient (R). The observed reference is marked by a black circle on the x-axis.

a significant advance beyond the narrow prediction scope prevalent in prior work.

The tri-hybrid feature fusion strategy proved highly effective, demonstrating that integrating XGBoost leaf encodings (capturing regime-aware adsorption–desorption transitions), MLP-derived hidden features (learning continuous nonlinear transformations), and raw input features provides complementary strengths unattainable by any single paradigm. These heterogeneous representations were concatenated into a unified embedding and subsequently refined by a transformer-based attention module, enabling dynamic modeling of higher-order target-dependent feature interactions. Comparative analysis revealed consistent superiority over five baseline models across all metrics for supply temperature, supply humidity, and cooling capacity, while achieving the highest R^2 and lowest MSE/RMSE for coefficient of performance. Notably, single-paradigm predictors exhibited substantial degradation for complex outputs: XGBoost became unstable for cooling capacity ($R^2 = 0.729$), whereas the proposed model maintained robust performance ($R^2 = 0.988$).

Implementation of 5-fold cross-validation with metrics reported as fold-averaged values and standard deviations directly addressed the generalization gap documented in the literature. Low fold-to-fold variability ($\sigma_{R^2} = 0.003$ for COP, $\sigma_{RMSE} = 0.004\,°C$ for $T_{s,out}$) confirms stable performance across data partitions, providing reliable estimates of real-world applicability in contrast to prior studies lacking rigorous validation.

SHAP analysis revealed physically consistent feature importance, validating model reasoning. Regeneration temperature dominated supply temperature prediction (SHAP value 0.32), consistent with its role

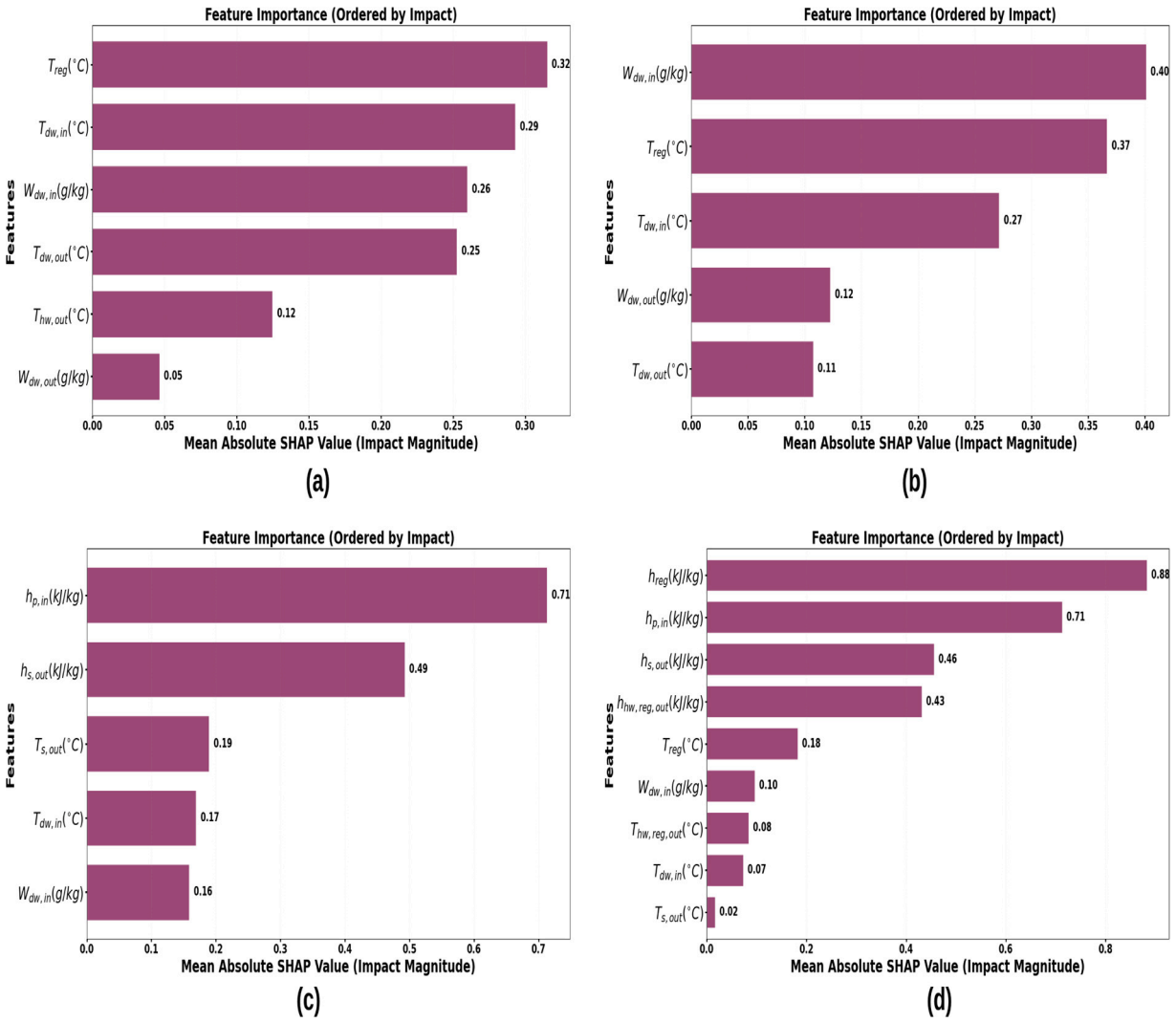


Fig. 10. Global feature importance ranking based on mean absolute SHAP values for (a) $T_{s,out}$, (b) $W_{s,out}$, (c) CC, and (d) COP. Features are ranked by the magnitude of their impact on the system performance predictions.

in controlling dehumidification and evaporative cooling. Inlet humidity governed supply humidity prediction, reflecting moisture adsorption driven by concentration gradients. Cooling capacity was primarily influenced by process inlet enthalpy, aligning with its definition as enthalpy difference between inlet and outlet streams. Most significantly, COP prediction was dominated by regeneration enthalpy rather than process-side conditions, confirming that desiccant system efficiency is primarily governed by regeneration energy requirements. This transparency enables physical validation and informed optimization while providing engineering trust through verifiable alignment with thermodynamic principles.

Several limitations warrant acknowledgment and future investigation. Extrapolation capability beyond training conditions ($T_{reg} > 90\,°C$, $W_{dw,in} > 20\,g/kg$) remains unverified; physics-informed constraints could ensure physically plausible predictions outside the training envelope. The current framework neglects temporal correlations; incorporating recurrent or attention mechanisms could capture transient behavior during dynamic loads. Computational efficiency for real-time control requires assessment, with model compression techniques offering pathways to reduce inference latency. Validation across different system configurations (alternative desiccant materials, Maisotsenko cycle integration, hybrid designs) and climate zones would establish broader generalizability. Finally, integrating Bayesian approaches would enable probabilistic predictions with uncertainty estimates for risk-aware decision-making.

CRediT authorship contribution statement

Habeb Al-Sameai: Writing – original draft, Visualization, Coding, Methodology, Investigation, Conceptualization. **Sibghat Ullah:** Writing – original draft, Visualization, Formal analysis, Data curation. **Radhwan A.A. Saleh:** Writing – original draft, Visualization, Coding, Methodology, Investigation, Conceptualization. **Mustafa Ghaleb:** Writing – review & editing, Supervision. **Tauqir Nasir:** Writing – review & editing. **Müslüm Arıcı:** Writing – review & editing, Project administration. **Zead Saleh:** Writing – review & editing, Project administration. **Muzaffar Ali:** Writing – review & editing, Supervision, Resources, Project administration.

Declaration of competing interest

The authors declare that they have no known competing financial interests or personal relationships that could have appeared to influence the work reported in this paper.

Data availability

Data will be made available on request.

References

[1] P. Vivekh, M. Kumja, D. Bui, K. Chua, Recent developments in solid desiccant coated heat exchangers – A review, Appl. Energy 229 (2018) 778–803, http://dx.doi.org/10.1016/j.apenergy.2018.08.041, URL: https://www.sciencedirect.com/science/article/pii/S0306261918311978.

[2] D. Ürge-Vorsatz, L.F. Cabeza, S. Serrano, C. Barreneche, K. Petrichenko, Heating and cooling energy trends and drivers in buildings, Renew. Sustain. Energy Rev. 41 (2015) 85–98, http://dx.doi.org/10.1016/j.rser.2014.08.039, URL: https://www.sciencedirect.com/science/article/pii/S1364032114007151.

[3] S.J. Oh, K.C. Ng, K. Thu, M.K. Ja, M.R. Islam, W. Chun, K.J.E. Chua, Studying the performance of a dehumidifier with adsorbent coated heat exchangers for tropical climate operations, Sci. Technol. Built Environ. 23 (1) (2017) 127–135, http://dx.doi.org/10.1080/23744731.2016.1218234.

[4] X. Cao, X. Dai, J. Liu, Building energy-consumption status worldwide and the state-of-the-art technologies for zero-energy buildings during the past decade, Energy Build. 128 (2016) 198–213, http://dx.doi.org/10.1016/j.enbuild.2016.06.089, URL: https://www.sciencedirect.com/science/article/pii/S0378778816305783.

[5] A. Ditta, A.N. Tabish, M.A. Mujtaba, M. Amjad, A.A. Yusuf, G.Q. Chaudhary, L. Razzaq, A. Abdelrahman, M.A. Kalam, Experimental investigation of a hybrid configuration of solar thermal collectors and desiccant indirect evaporative cooling system, Front. Energy Res. Volume 10 - 2022 (2022) http://dx.doi.org/10.3389/fenrg.2022.979942, URL: https://www.frontiersin.org/journals/energy-research/articles/10.3389/fenrg.2022.979942.

[6] S. Ullah, M. Ali, Performance assessment of solar desiccant air conditioning system under multiple controlled climatic zones of Pakistan, Energies 16 (19) (2023) http://dx.doi.org/10.3390/en16196914, URL: https://www.mdpi.com/1996-1073/16/19/6914.

[7] U. Eicker, U. Schürger, M. Köhler, T. Ge, Y. Dai, H. Li, R. Wang, Experimental investigations on desiccant wheels, Appl. Therm. Eng. 42 (2012) 71–80, http://dx.doi.org/10.1016/j.applthermaleng.2012.03.005, URL: https://www.sciencedirect.com/science/article/pii/S1359431112001603. Heat Powered Cycles Conference, 2009.

[8] S. Ullah, M. Ali, A. Ditta, G.Q. Chaudhary, H. Ali, S. He, Effect of critical parameters on the performance of integrated climate controlled solar desiccant air conditioning system, Energy Rep. 14 (2025) 2451–2463, http://dx.doi.org/10.1016/j.egyr.2025.09.024, URL: https://www.sciencedirect.com/science/article/pii/S2352484725005402.

[9] T. Ge, F. Ziegler, R. Wang, A mathematical model for predicting the performance of a compound desiccant wheel (A model of compound desiccant wheel), Appl. Therm. Eng. 30 (8) (2010) 1005–1015, http://dx.doi.org/10.1016/j.applthermaleng.2010.01.012, URL: https://www.sciencedirect.com/science/article/pii/S1359431110000189.

[10] G. Angrisani, F. Minichiello, M. Sasso, Improvements of an unconventional desiccant air conditioning system based on experimental investigations, Energy Convers. Manage. 112 (2016) 423–434, http://dx.doi.org/10.1016/j.enconman.2016.01.013, URL: https://www.sciencedirect.com/science/article/pii/S0196890416000297.

[11] T. Elmer, M. Worall, S. Wu, S. Riffat, An experimental study of a novel integrated desiccant air conditioning system for building applications, Energy Build. 111 (2016) 434–445, http://dx.doi.org/10.1016/j.enbuild.2015.11.065, URL: https://www.sciencedirect.com/science/article/pii/S037877881530428X.

[12] A. Khalid, M. Mahmood, M. Asif, T. Muneer, Solar assisted, pre-cooled hybrid desiccant cooling system for Pakistan, Renew. Energy 34 (1) (2009) 151–157, http://dx.doi.org/10.1016/j.renene.2008.02.031, URL: https://www.sciencedirect.com/science/article/pii/S0960148108000827.

[13] L. Chen, S. Chen, L. Liu, B. Zhang, Experimental investigation of precooling desiccant-wheel air-conditioning system in a high-temperature and high-humidity environment, Int. J. Refrig. 95 (2018) 83–92, http://dx.doi.org/10.1016/j.ijrefrig.2018.08.015, URL: https://www.sciencedirect.com/science/article/pii/S0140700718303116.

[14] M. Karami, S. Delfani, A. Noroozi, Performance characteristics of a solar desiccant / M - cycle air - conditioning system for the buildings in hot and humid areas, Asian J. Civ. Eng. 21 (2) (2020) 189–199, http://dx.doi.org/10.1007/s42107-019-00197-z.

[15] J. Lin, R. Wang, M. Kumja, T. Bui, K. Chua, Modelling and experimental investigation of the cross-flow dew point evaporative cooler with and without dehumidification, Appl. Therm. Eng. 121 (2017) 1–13, http://dx.doi.org/10.1016/j.applthermaleng.2017.04.047, URL: https://www.sciencedirect.com/science/article/pii/S1359431117313236.

[16] S. Muthu, P. Talukdar, S. Jain, Effect of regeneration section angle on the performance of a rotary desiccant wheel, J. Therm. Sci. Eng. Appl. 8 (1) (2015) 011013, http://dx.doi.org/10.1115/1.4030966.

[17] S. Tian, X. Su, H. Li, Y. Huang, Using a coupled heat pump desiccant wheel system to improve indoor humidity environment of nZEB in Shanghai: Analysis and optimization, Build. Environ. 206 (2021) 108391, http://dx.doi.org/10.1016/j.buildenv.2021.108391, URL: https://www.sciencedirect.com/science/article/pii/S0360132321007885.

[18] Z. Ma, X. Chang, T. Zhang, X. Liu, B. Guan, On-site measurement and optimization of energy efficiency of the cascading desiccant wheel deep dehumidification systems in the lithium-ion battery manufacturing factory, Energy Build. 304 (2024) 113833, http://dx.doi.org/10.1016/j.enbuild.2023.113833, URL: https://www.sciencedirect.com/science/article/pii/S0378778823010630.

[19] E. Van den Bulck, J.W. Mitchell, S.A. Klein, The use of dehumidifiers in desiccant cooling and dehumidification systems, J. Heat Transf. 108 (3) (1986) 684–692, http://dx.doi.org/10.1115/1.3246990.

[20] S. Ullah, M. Ali, M.F. Sheikh, G.Q. Chaudhary, L. Kerbache, Performance predication of a solar assisted desiccant air conditioning system using radial basis function neural network: An integrated machine learning approach, Heliyon 10 (9) (2024) e29777, http://dx.doi.org/10.1016/j.heliyon.2024.e29777.

[21] S.S. Salins, S. Kumar, S.V.K. Reddy, A.V. Kuniyil, S.S. Kumar, Sustainable energy techniques adapted in buildings to regulate moisture transport and enhance thermal comfort: A review, Int. J. Air-Cond. Refrig. 29 (03) (2021) 2130003, http://dx.doi.org/10.1142/S2010132521300032.

[22] D. Jani, M. Mishra, P. Sahoo, Application of artificial neural network for predicting performance of solid desiccant cooling systems – a review, Renew. Sustain. Energy Rev. 80 (2017) 352–366, http://dx.doi.org/10.1016/j.rser.2017.05.169, URL: https://www.sciencedirect.com/science/article/pii/S1364032117308079.

[23] A. Zendehboudi, A. Tatar, X. Li, A comparative study and prediction of the liquid desiccant dehumidifiers using intelligent models, Renew. Energy 114 (2017) 1023–1035, http://dx.doi.org/10.1016/j.renene.2017.07.078, URL: https://www.sciencedirect.com/science/article/pii/S0960148117307061.

[24] F. Comino, D. Guijo-Rubio, M. Ruiz de Adana, C. Hervás-Martínez, Validation of multitask artificial neural networks to model desiccant wheels activated at low temperature, Int. J. Refrig. 100 (2019) 434–442, http://dx.doi.org/10.1016/j.ijrefrig.2019.02.002, URL: https://www.sciencedirect.com/science/article/pii/S0140700719300520.

[25] D. Jani, M. Mishra, P.K. Sahoo, Performance prediction of solid desiccant–vapor compression hybrid air-conditioning system using artificial neural network, Energy 103 (2016) 618–629.

[26] J. Cejudo, R. Moreno, A. Carrillo, Physical and neural network models of a silica-gel desiccant wheel, Energy Build. 34 (8) (2002) 837–844, http://dx.doi.org/10.1016/S0378-7788(02)00100-7, URL: https://www.sciencedirect.com/science/article/pii/S0378778802001007. REHVA Scientific.

[27] H. Parmar, D. Hindoliya, Artificial neural network based modelling of desiccant wheel, Energy Build. 43 (12) (2011) 3505–3513, http://dx.doi.org/10.1016/j.enbuild.2011.09.016, URL: https://www.sciencedirect.com/science/article/pii/S037877881100404X.

[28] S. De Antonellis, M. Intini, C.M. Joppolo, Desiccant wheels effectiveness parameters: Correlations based on experimental data, Energy Build. 103 (2015) 296–306, http://dx.doi.org/10.1016/j.enbuild.2015.06.041, URL: https://www.sciencedirect.com/science/article/pii/S0378778815300670.

[29] M.M. Rafique, S. Rehman, Renewable and sustainable air conditioning, in: C. Ghenai, T. Salameh (Eds.), Sustainable Air Conditioning Systems, IntechOpen, London, 2018, http://dx.doi.org/10.5772/intechopen.73166.

[30] Y. Lee, S. Park, S. Kang, Performance analysis of a solid desiccant cooling system for a residential air conditioning system, Appl. Therm. Eng. 182 (2021) 116091, http://dx.doi.org/10.1016/j.applthermaleng.2020.116091, URL: https://www.sciencedirect.com/science/article/pii/S1359431120335717.

[31] G.A. Shaik, V. Prabakaran, M.K. Jagirdar, Deep dehumidification using novel cycle-operated desiccant-coated heat exchangers driven by an ultra-low-grade heat source, Energy Convers. Manage. 349 (2026) 120836, http://dx.doi.org/10.1016/j.enconman.2025.120836, URL: https://www.sciencedirect.com/science/article/pii/S0196890425013603.

[32] Y.E. Güzelel, U. Olmuş, O. Büyükalaca, Simulation of a desiccant air-conditioning system integrated with dew-point indirect evaporative cooler for a school building, Appl. Therm. Eng. 217 (2022) 119233, http://dx.doi.org/10.1016/j.applthermaleng.2022.119233, URL: https://www.sciencedirect.com/science/article/pii/S1359431122011632.

[33] U. Olmuş, Y.E. Güzelel, O. Büyükalaca, Seasonal analysis of a desiccant air-conditioning system supported by water-cooled PV/T units, Energy Build. 291 (2023) 113101, http://dx.doi.org/10.1016/j.enbuild.2023.113101, URL: https://www.sciencedirect.com/science/article/pii/S0378778823003316.

[34] M. Abdelgaied, M.A. Saber, M. Bassuoni, A.M. Khaira, Solid desiccant air conditioning system using desiccant dehumidifiers with cooling technique and thermal recovery unit: Experimental investigation and performance analysis, J. Clean. Prod. 421 (2023) 138387, http://dx.doi.org/10.1016/j.jclepro.2023.138387, URL: https://www.sciencedirect.com/science/article/pii/S0959652623025453.

[35] R. Tariq, M. Ali, N.A. Sheikh, M.W. Shahzad, B.B. Xu, Deep learning artificial intelligence framework for sustainable desiccant air conditioning system: Optimization towards reduction in water footprints, Int. Commun. Heat Mass Transfer 140 (2023) 106538, http://dx.doi.org/10.1016/j.icheatmasstransfer.2022.106538, URL: https://www.sciencedirect.com/science/article/pii/S0735193322006601.

[36] S.A. Bhat, U. Sajjad, I. Hussain, W.-M. Yan, H.M. Raza, H.M. Ali, M. Sultan, H. Omar, M.W. Azam, F. Bozzoli, N.-F. Huang, Experiments and modeling on thermal performance evaluation of standalone and M-cycle based desiccant air-conditioning systems, Energy Rep. 11 (2024) 1445–1454, http://dx.doi.org/10.1016/j.egyr.2024.01.019, URL: https://www.sciencedirect.com/science/article/pii/S2352484724000167.

[37] M. Kassim, M. Merzouk, N. Kasbadji Merzouk, L. Merabti, W. Taane, F. Bouzeffour, M. Ounnar, D. Belkacemi, Experimental study and simulation of a solid desiccant cooling system installed in northern Algeria, Energy Build. 324 (2024) 114943, http://dx.doi.org/10.1016/j.enbuild.2024.114943, URL: https://www.sciencedirect.com/science/article/pii/S0378778824010594.

[38] J. Srimuk, S. Chirarattananon, P. Chaiwiwatworakul, A. Nathakaranakule, P. Rakkwamsuk, S. Chiarakorn, An experiment and simulation on a solar-regenerated dehumidifier fabricated from composite desiccant coated fin-tube heat exchanger, Appl. Therm. Eng. 245 (2024) 122780, http://dx.doi.org/10.1016/j.applthermaleng.2024.122780, URL: https://www.sciencedirect.com/science/article/pii/S1359431124004484.

[39] B. Yang, C. Wang, X. Ji, J. Nie, R. Zhang, Y. Li, Q. Chen, A solar-assisted regenerative desiccant air conditioning with indirect evaporative cooling for humid climate region, Appl. Therm. Eng. 243 (2024) 122598, http://dx.doi.org/10.1016/j.applthermaleng.2024.122598, URL: https://www.sciencedirect.com/science/article/pii/S1359431124002667.

[40] W. Chen, X. Cui, Z. Huang, Y. Shao, K. Chua, Developing an integrated solid desiccant dehumidifier and dew-point evaporative cooler for green air conditioning, J. Build. Eng. 96 (2024) 110404, http://dx.doi.org/10.1016/j.jobe.2024.110404, URL: https://www.sciencedirect.com/science/article/pii/S2352710224019727.

[41] I. Hussain, U. Sajjad, S.A. Bhat, N. Abbas, A. Ali, M. Sultan, H.M. Ali, K. Hamid, W.-M. Yan, N. Rubab, Potential evaluation of AI-based surrogate models to find the robust and optimal method for thermal performance assessment of desiccant air-conditioning systems, Energy Convers. Manag.: X 25 (2025) 100782, http://dx.doi.org/10.1016/j.ecmx.2024.100782, URL: https://www.sciencedirect.com/science/article/pii/S2590174524002605.

[42] Y. Chen, Z. Chen, Y. Liang, L. Li, Z. Wang, Performance analysis and optimization of two-stage desiccant wheel cooling systems in low-latitude island with hot and humid climate, Case Stud. Therm. Eng. 78 (2026) 107714, http://dx.doi.org/10.1016/j.csite.2026.107714, URL: https://www.sciencedirect.com/science/article/pii/S2214157X26000766.

[43] S.J. Kline, Describing uncertainties in single-sample experiments, Mech. Eng. 75 (1953) 3–8, URL: https://api.semanticscholar.org/CorpusID:115904659.

[44] J. Holman, Experimental Methods for Engineers, McGraw-Hill Education, 2011, URL: https://books.google.com.tr/books?id=CZWFZwEACAAJ.

[45] L. Breiman, Random forests, Mach. Learn. 45 (1) (2001) 5–32, http://dx.doi.org/10.1023/A:1010933404324.

[46] T. Chen, C. Guestrin, XGBoost: A scalable tree boosting system, in: Proceedings of the 22nd ACM SIGKDD International Conference on Knowledge Discovery and Data Mining, KDD '16, Association for Computing Machinery, New York, NY, USA, 2016, pp. 785–794, http://dx.doi.org/10.1145/2939672.2939785.

[47] A.J. Smola, B. Schölkopf, A tutorial on support vector regression, Stat. Comput. 14 (3) (2004) 199–222.

[48] K. Hornik, M. Stinchcombe, H. White, Multilayer feedforward networks are universal approximators, Neural Netw. 2 (5) (1989) 359–366, http://dx.doi.org/10.1016/0893-6080(89)90020-8, URL: https://www.sciencedirect.com/science/article/pii/0893608089900208.

[49] X. Huang, A. Khetan, M. Cvitkovic, Z.S. Karnin, TabTransformer: Tabular data modeling using contextual embeddings, 2020, arXiv abs/2012.06678. URL: https://api.semanticscholar.org/CorpusID:229156048.

[50] A. Vaswani, N. Shazeer, N. Parmar, J. Uszkoreit, L. Jones, A.N. Gomez, L. Kaiser, I. Polosukhin, Attention is all you need, in: Proceedings of the 31st International Conference on Neural Information Processing Systems, NIPS '17, Curran Associates Inc., Red Hook, NY, USA, 2017, pp. 6000–6010.

[51] J. Ba, J.R. Kiros, G.E. Hinton, Layer normalization, 2016, arXiv abs/1607.06450. URL: https://api.semanticscholar.org/CorpusID:8236317.

[52] K. He, X. Zhang, S. Ren, J. Sun, Deep residual learning for image recognition, in: 2016 IEEE Conference on Computer Vision and Pattern Recognition, CVPR, 2015, pp. 770–778, URL: https://api.semanticscholar.org/CorpusID:206594692.

[53] N. Khosravi, D. Aydin, Investigation of a storage type solar-driven solid desiccant cooling system, Gazi Üniv. Fen Bilim. Derg. Part C: Tasanm Teknol. 9 (3) (2021) 463–477, http://dx.doi.org/10.29109/gujsc.943429.

[54] F. Comino, J. Castillo González, F. Navas-Martos, M. Ruiz de Adana, Experimental energy performance assessment of a solar desiccant cooling system in Southern Europe climates, Appl. Therm. Eng. 165 (2020) 114579, http://dx.doi.org/10.1016/j.applthermaleng.2019.114579, URL: https://www.sciencedirect.com/science/article/pii/S1359431119350872.

[55] L. Lai, X. Wang, G. Kefayati, E. Hu, Performance evaluation of a solar powered solid desiccant evaporative cooling system with different recirculation air ratios, Energy Build. 270 (2022) 112273, http://dx.doi.org/10.1016/j.enbuild.2022.112273, URL: https://www.sciencedirect.com/science/article/pii/S0378778822004443.

[56] S. Belguith, Z. Meddeb, R. Ben Slama, Performance analysis of desiccant cooling systems in a hot and dry climate, Euro-Mediterr. J. Environ. Integr. 6 (1) (2020) 2, http://dx.doi.org/10.1007/s41207-020-00210-x.

[57] R. Kousar, M. Ali, N.A. Sheikh, S.I. ul Haq Gilani, S. Khushnood, Holistic integration of multi-stage dew point counter flow indirect evaporative cooler with the solar-assisted desiccant cooling system: A techno-economic evaluation, Energy Sustain. Dev. 62 (2021) 163–174, http://dx.doi.org/10.1016/j.esd.2021.04.005, URL: https://www.sciencedirect.com/science/article/pii/S097308262100051X.